Meso to macro connections to capture fatigue damage in cemented materials

Vinh T. Le [a], Ha H. Bui [a,*], Giang D. Nguyen [b], Jayantha Kodikara [c], Didier Bodin [d], James Grenfell [d]

[a] Department of Civil Engineering, Monash University, Australia
[b] School of Civil, Environmental & Mining Engineering, The University of Adelaide, Australia
[c] ARC Industrial Transformation Research Hub (ITRH) – SPARC Hub, Department of Civil Engineering, Monash University, Australia
[d] ARRB Group Ltd, Port Melbourne, VIC 3207, Australia

ARTICLE INFO

ABSTRACT

Fatigue-induced damage is a common issue in cemented materials, involving the progressive formation and complicated propagation of fatigue cracks. These cracks typically localise on weak or fracture planes, leading to inhomogeneous deformation within the material. Thus, accurately predicting the fatigue phenomenon becomes challenging due to the material's inhomogeneity and the complex evolution of cracks, from initiation to propagation and eventual failure. To address this challenge, this paper presents a constitutive model that accounts for strain discontinuity across fracture planes by employing kinematic enrichment. This enhancement facilitates interaction between the material responses of cracks and the outer bulk, thereby contributing to the overall macro behaviour of the materials. Moreover, the proposed model incorporates a new cohesive-frictional fatigue model that couples damage mechanics and bounding surface plasticity to describe the fatigue behaviour of fracture planes/cracks. Since the proposed model features a characteristic length scale, it exhibits size-dependent behaviour and helps overcome the issue of mesh dependence. The model's validity is demonstrated through its ability to capture nonlinear fatigue damage under constant/variable cyclic loading and to simulate the propagation of fatigue fracture process zones. Furthermore, the model effectively captures the significant influence of stress amplitudes on the fatigue lives of materials, making it an essential tool for predicting and mitigating fatigue-induced damage in cemented materials.

1. Introduction

Many engineering structures are made of cementitious materials such as pavement, bridges, concrete foundations of wind power towers and high-speed railways. However, during their service lifetimes, these structures experience gradual degradations and eventually failures due to fatigue-induced damage under repetitive loading. Generally, the fatigue phenomenon is a complicated process, but it can be described by three distinct phases: crack initiation, stable crack propagation and rapid rupture [25,68,69]. In cemented materials, fatigue cracks initiate at the material flaws, which are pre-existing micro-cracks at the interfaces (weak surfaces) between aggregates and cement paste or the mortar matrix [36,54]. Upon fatigue loads, these microcracks continue to propagate along the interfaces, resulting in the deterioration of materials [18,59,66]. Therefore, the cohesion and frictional behaviour of

the interfaces in materials play an essential role in contributing to the dissipated fatigue mechanism [7]. At the macro behaviour, this fatigue dissipation is reflected by hysteretic loops forming by the unloading and reloading paths. The more significant area of the hysteresis loops is, the more energy dissipates, which was observed in many experimental studies [8,12,21,26].

Since the cohesive-frictional behaviour of the weak interfaces inside cemented materials is the fundamental mechanism governing the deterioration due to fatigue damage, it should be considered a foundation for developing constitutive models for fatigue issues. However, certain phenomenological constitutive models do not follow this pattern. Instead, they use merely macromechanical responses and omit the underlying mechanisms. For instance, Sima et al. [58], Aslani and Jowkarmeimandi [3], Breccolotti et al. [9], Chen et al. [11], Zhang et al. [77], Tsutsumi and Fincato [63] developed empirical models that relate stress and strain responses based on experimental results. These models

---

* Corresponding author.
  E-mail address: ha.bui@monash.edu (H.H. Bui).

Nomenclature

Ω	Representative volume element (RVE)
Ω_k	Volume of fracture plane/crack k $(k = 1, 2)$
Ω_o	Volume of the bulk material outside cracks
l_k	Thickness of cracks
A_k	Area of cracks
$\mathbf{n}_k$	Normal vector of crack k
$\mathbf{R}_k$	Transformation matrix of crack k from global to local coordinate system
$\mathbf{r}_k$	Residual vector of crack k
$\boldsymbol{\varepsilon}$	Average strain vector
$\boldsymbol{\varepsilon}_o$	Strain vector outside the cracks
$\boldsymbol{\varepsilon}_{ik}$	Strain vector on the crack k
$\boldsymbol{\sigma}$	Average stress vector
$\boldsymbol{\sigma}_o$	Stress vector outside the cracks
$\boldsymbol{\sigma}_{ik}$	Stress vector on the crack k
$\mathbf{a}_o$	Elastic stiffness of material in matrix form
$\mathbf{K}_k^t$	Tangent stiffness of crack k in global coordinate system
$\mathbf{K}_c^s$	Secant stiffness of crack in local coordinate system
$\mathbf{K}_{ck}^s$	Secant stiffness of crack k in local coordinate system
K_n, K_s	Elastic normal and shear stiffness of crack
$\mathbf{u}_k$	Total displacement jump of crack k in global coordinate system
$\mathbf{u}_c$	Total displacement jump of crack in local coordinate system
$\mathbf{t}_c = [t_n \ t_{s1} \ t_{s2}]^T$	Traction of crack in local coordinate system
$\mathbf{t}_{ck} = [t_{k,n} \ t_{k,s1} \ t_{k,s2}]^T$	Traction of crack k in local coordinate system
$\mathbf{u}_c = [u_n \ u_{s1} \ u_{s2}]^T$	Total displacement jump of crack in local coordinate system
$\mathbf{u}_{ck} = [u_{k,n} \ u_{k,s1} \ u_{k,s2}]^T$	Total displacement jump of crack k in local coordinate system
$\mathbf{u}_c^e$	Elastic displacement jump of crack in local coordinate system
$\mathbf{u}_c^p = [u_n^p \ u_{s1}^p \ u_{s2}^p]^T$	Plastic displacement jump of crack in local coordinate system
$\mathbf{u}_c^f = [u_n^f \ u_{s1}^f \ u_{s2}^f]^T$	Fatigue displacement jump of crack in local coordinate system
y	Bounding surface
y_0	Subloading surface
ν	Poisson's ratio
f_t^0	Tensile strength of material
C^0	Cohesion of material
μ	Material internal friction coefficient
φ	Friction angle
α, β	Parameters controlling damage evolution
δ_s, δ_f	Relative displacement parameters for normalisation
ψ	Parameter controlling position of subloading surface
X_n	Kinematic hardening parameter
e_{do}	Elastic domain of subloading surface
Q, κ	Parameters controlling the magnitude of fatigue flow rule
S_I, S_K	Softening moduli on the subloading and reference surfaces, respectively
m_1, m_2	Parameters controlling fatigue damage increment
u_{ps}	Accumulated plastic displacement parameter
$\dot{D}_s, \dot{D}_f$	Incremental static and fatigue damages of crack, respectively
G_c	Fracture energy
m_{jump}, C_{jump}	Calibration parameters for cycle jump technique
N_f, N_{fl}	Cycles to reach 50% of initial modulus and to reach failure, respectively
FPZ	Fracture process zone
FS	Flexural strength
S-N curves	Stress levels – fatigue lives curves
CMOD, CTOD	Crack mouth opening displacement, Crack tip opening displacement

aim to simulate low/high-cycle fatigue hysteresis behaviour under straightforward loading scenarios (uniaxial cyclic tension and/or compression loading paths). As a result, the testing conditions on which those models are developed and calibrated place limits on their capabilities. As an alternative, fatigue-bonded contact models (FBCMs) integrated into the discrete element method (DEM) can successfully capture both microstructural changes and fatigue degradation at contact levels [49,60,79,80]. The primary concepts behind these models are to relate the rate of bonded contact deteriorations (i.e. reduction in cohesion and tensile strength of bonded contacts or degradation in bonded diameters) to the number of cycles or simulation time increments. Understanding the mechanism of fatigue failure or the impact of microstructural changes on fatigue lives in cemented materials can be accomplished with FBCMs. However, the high computational cost can be a significant drawback that prevents these models from being widely applied to large-scale simulations with thousands of cycles.

Another approach to modelling fatigue problems is continuum modelling which can be divided into two categories: cyclic cohesive zone models (CCZMs) and fatigue damage mechanics models. The main building stone of the first group is the traction-separation relation, which is used to characterise crack initiation and to describe the fracture process zone (FPZ) ahead of the crack tip [1,20,71,73,78]. Additionally, this traction-separation law offers helpful ways to depict the development of fatigue cracks and hysteresis behaviour. Therefore, different hysteretic cohesive laws with varying stiffnesses depending on the direction of loading (unloading/reloading) were proposed and developed by Nguyen et al. [50], Eliáš and Le [15], Jin and Huang [24]. These

models, however, adopted linear unloading in the tension regime without irrecoverable separation or strain. By contrast, Yang et al. [75] proposed a CCZM with polynomial functions for unloading and reloading stiffnesses, wherein damage accumulation during unloading is allowed to occur. Nevertheless, the above cohesive models assumed fatigue damage development to be independent of the softening branch of the monotonic envelope curve, thereby treating static and fatigue damage separately. Despite the practical usefulness and simplicity in the implementation of CCZMs into a numerical method such as the extended finite element method (XFEM) [23,24,30,74,78], the application of CCZMs is restricted. This limitation is due to the approach having potential problems with the unphysical stress-locking phenomenon in numerical simulations of FPZ evolution. The phenomenon stems from using and fixing the orientation of a single crack. Therefore, CCZMs require numerical treatments, for example, the need for the suitably dense discretisation of the finite element method (FEM) model. Nevertheless, such one-crack models cannot fully resolve the stress-locking problem under changes in loading paths where multiple cracks may initiate and propagate.

The second group is based on the theory of damage mechanics, which considers the progressive growth and coalescence of microcracks that cause material degradation by using scalar or tensorial damage variables. Marigo [41] first developed a fatigue damage model for elastic materials using the loading–unloading irreversibility concept for accounting for damage accumulation even at loading levels below the material strength. This study couples two damages together by calculating the fatigue damage rate as the static damage rate multiplied by the

viscous function. Marigo's research has since significantly influenced subsequent studies, but they differ in terms of damage variables and gauge functions used. For instance, the majority of models are written in strain space with tensorial damage variable [2,51] or scalar damage one [39]. Meanwhile, some models work in effective stress space [37,55,76] with two different types of damage, one in tension and one in compression. Although sufficiently well-capturing fatigue responses of materials, these classical constitutive models are developed based on an assumption of homogeneous deformation of materials. Therefore, the models are not physically meaningful beyond the onset of localisation, where strong discontinuities take place. As a result, the reliabilities of those models are questionable when dealing with softening and localisation in the analysis of boundary value problems (BVPs).

To deal with these issues, microplane fatigue models can be a more reliable framework [5,27], wherein the fatigue damage evolution is linked with cumulative volumetric/shear strain to account for dissipative mechanisms on the weak interfaces within cemented materials. The basis of this method is to capture the macroscopic behaviour of the material by incorporating numerous weak planes in all directions, and hence can handle complicated loading paths with multiple cracks. Even though these models map all the effects of failure planes to a single macro stress–strain relation, they still do not take into account the mechanism of localised failure. In other words, these models still use the homogeneous deformation assumption implicitly. Besides, the numerical accuracy of the approach is highly dependent on the massive number of all microplanes, in which numerous internal variables need to be stored and updated in each step of the finite element implementation. Consequently, the computational demands of the microplane model have been considered excessive.

In this study, the cohesive-frictional behaviour of the weak interfaces in cemented materials is incorporated explicitly and systematically to obtain a size-dependent fatigue model. The high strain discontinuity across fracture planes is accounted for, by kinematic enrichments that adhere to the double-scale constitutive framework [42,44,46,48]. These enhancements enable the introduction of a novel cohesive fatigue model to describe the material responses on fracture planes when the fatigue cracks initiate and develop. This new fatigue model is developed based on the coupling of damage mechanics and bounding surface plasticity. Furthermore, the cohesive fatigue model naturally provides both the onset and orientation of the fracture planes, which depend on stress states and material properties. The key features of the proposed model include: (i) Both the linear elasticity response of intact bulk material and the nonlinear inelasticity of material response on the fracture planes are directly considered; (ii) Due to the inherent appearance of a length scale in formulation, the model exhibits size-dependent behaviour and automatically ensures numerical convergence upon discretisation refinement; (iii) The model incorporates two different fatigue failure mechanisms in the tension-shear and compression-shear regimes; (iv) Static and fatigue damages (i.e., quasi-static and cyclic induced damages) are coupled together, hence allowing for a smooth transition from static to fatigue damages and vice versa in a unified way.

The paper is organised as follows. Key features to formulate the double-scale framework together with a novel cohesive fatigue model are presented in Section 2. Then, the model implementation is given in detail in Section 3. This is followed by the model behaviour and validation at the material level in Section 4. Along with this, Section 5 presents the material analysis at structural levels. Finally, the main conclusion of this study is presented in Section 6.

2. Double-scale modelling of fatigue-induced fractures

This section presents the double-scale continuum constitutive framework with two fracture planes (two cracks). The general ideas and key formulations of this framework are first presented, followed by the novel cohesive-frictional fatigue model used to describe the material responses of fracture planes.

2.1. Double-scale constitutive framework

As presented in Section 1, fatigue damage in cemented materials typically occurs at interfaces between aggregates, and cement paste or the mortar matrix. This damage leads to the propagation of cracks along interfaces, and these surfaces can be considered weak planes or fracture planes surrounded by intact material. From the modelling viewpoint, there is a need for a reliable constitutive model which can account for the material responses on fracture planes, and the behaviour of the surrounding intact material. More importantly, the behaviour on and outside these fracture planes needs to interact with each other to contribute to the overall macro response of the damaged material. To accomplish this, the double-scale framework, developed by Nguyen, Einav and Korsunsky [44], Nguyen et al. [46]; Nguyen et al. [48]; Nguyen and Bui [42], is employed. Unlike classical constitutive models, wherein deformation is assumed to be homogeneous over a unit volume, the double-scale framework defines a new volume element crossed by localisation bands. The width of these bands can be finite for granular materials (i.e. the finite thickness of shear bands) or infinitesimal for quasi-brittle materials (i.e. idealised-zero thickness of FPZ). This assumption is reasonable because, in quasi-brittle materials, the FPZ thickness is often very small and has been accounted for in the fracture energy. In particular, dissipation inside this FPZ is lumped on the fracture energy, and cohesive-frictional models are used to describe the FPZ behaviour. These models employ a traction-separation law, in which separation is the relative displacements between two sides of the very thin FPZ [16].

The double-scale framework was originally proposed for a single localisation band/crack within a representative volume element (RVE). However, when subjected to non-proportional loading conditions with changes in loading paths, using a single crack often suffers from stress-locking issues. To address this, Le et al. [31,32] developed the double-scale framework with two-embedded cracks (two-crack model), which enables the development and propagation of secondary cracks. The advantages of the two-crack model were demonstrated in these studies, as it effectively eliminates stress-locking issues and accurately captures macro-crack propagation under monotonic loadings. Therefore, this paper adopts the two-crack model to describe the fatigue responses of materials by incoporating a newly developed cohesive fatigue model.

We define an RVE Ω comprising two fracture planes Ω_k ($k = 1, 2$) and an outer bulk material Ω_o, as shown in Fig. 1. The fracture planes are characterised by a thickness l_k and an area A_k which is represented by the normal vector $\mathbf{n}_k$. The nominal size of the RVE can be defined as $L_k = \Omega_k/A_k$. The volume-averaged total strain rate can be decomposed into the outer and inner strain rates of the fracture planes using mixture theory:

$$\dot{\boldsymbol{\varepsilon}} = f_1\dot{\boldsymbol{\varepsilon}}_{i1} + f_2\dot{\boldsymbol{\varepsilon}}_{i2} + (1 - f_1 - f_2)\dot{\boldsymbol{\varepsilon}}_o \tag{1}$$

where $\dot{\boldsymbol{\varepsilon}}_o$ and $\dot{\boldsymbol{\varepsilon}}_{ik}$ denote the strain rate tensors outside and inside the fracture planes, respectively, and f_k represents the volume fraction of the fracture planes $f_k = l_k/L_k$.

Given very thin fracture planes in quasi-brittle materials ($l_k \ll L_k$), the strain rate tensor inside the fracture plane can be approximated [29,46]:

$$\dot{\boldsymbol{\varepsilon}}_{i1} = \frac{1}{l_1}\mathbf{n}_1\dot{\mathbf{u}}_1 \text{ and } \dot{\boldsymbol{\varepsilon}}_{i2} = \frac{1}{l_2}\mathbf{n}_2\dot{\mathbf{u}}_2 \tag{2}$$

where $\dot{\mathbf{u}}_k$ represents the displacement jump rate across the fracture planes.

Substituting Eq. (2) into Eq. (1), and using the relationship $f_k = l_k/L_k$, the averaged macro-strain rate tensor and the strain rate tensor outside the fracture planes can be calculated as:

$$\dot{\boldsymbol{\varepsilon}} = \frac{1}{L_1}\mathbf{n}_1\dot{\mathbf{u}}_1 + \frac{1}{L_2}\mathbf{n}_2\dot{\mathbf{u}}_2 + \left(1 - f_1 - f_2\right)\dot{\boldsymbol{\varepsilon}}_o \tag{3}$$
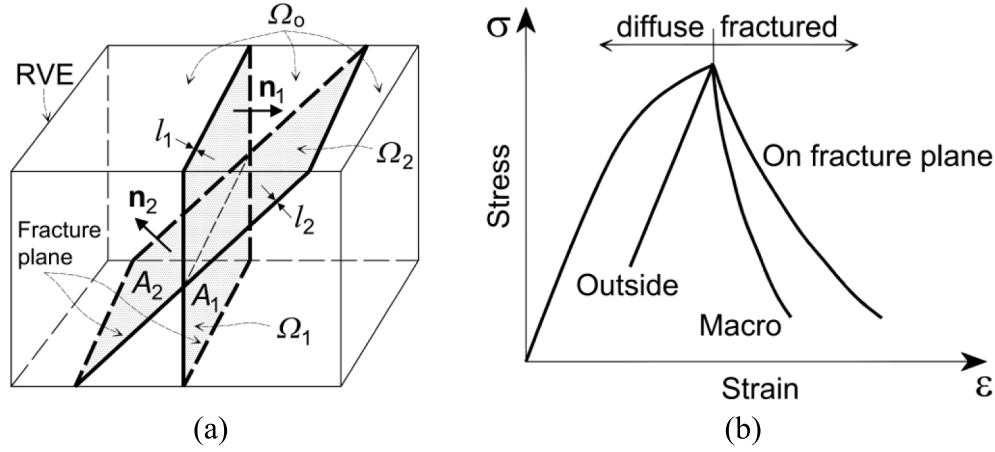
Fig. 1. (a) Illustration of an RVE with 2 fracture planes; (b) Material responses: pre-fracture and post-fracture. Before the onset of fracture planes, the material exhibits one stress–strain relationship known as the diffuse stage. However, after crack initiation occurs, three distinct behaviours can be observed within the damaged material. It is commonly assumed that dissipative processes occur only on fracture planes, while the surrounding bulk undergoes elastic unloading.

$$\dot{\boldsymbol{\varepsilon}}_o = \frac{1}{(1 - f_1 - f_2)} \left(\dot{\boldsymbol{\varepsilon}} - \frac{1}{L_1} \mathbf{n}_1 \dot{\mathbf{u}}_1 - \frac{1}{L_2} \mathbf{n}_2 \dot{\mathbf{u}}_2 \right) \tag{4}$$

To link the response of inside and outside the fracture planes with the overall behaviour of RVE, the virtual work equation (Hill-Mandel condition) is used. Specifically, the virtual work produced by the macro stress–strain rate must equal the total work done by the stress–strain rate inside and outside of the fracture planes:

$$\boldsymbol{\sigma}^T \dot{\boldsymbol{\varepsilon}} = f_1 \boldsymbol{\sigma}_{i1}^T \dot{\boldsymbol{\varepsilon}}_{i1} + f_2 \boldsymbol{\sigma}_{i2}^T \dot{\boldsymbol{\varepsilon}}_{i2} + (1 - f_1 - f_2) \boldsymbol{\sigma}_o^T \dot{\boldsymbol{\varepsilon}}_o \tag{5}$$

where $\boldsymbol{\sigma}_o$ and $\boldsymbol{\sigma}_{ik}$ are the stress tensors outside and inside the fracture planes, respectively.

Using Eqs. (1), (2) and conditions $f_1 \rightarrow 0$, $f_2 \rightarrow 0$ due to very thin fracture planes, Eq. (5) is rewritten as:

$$(\boldsymbol{\sigma}^T - \boldsymbol{\sigma}_o^T) \dot{\boldsymbol{\varepsilon}}_o + \frac{1}{L_1} (\boldsymbol{\sigma}^T \mathbf{n}_1 - \boldsymbol{\sigma}_{i1}^T \mathbf{n}_1) \dot{\mathbf{u}}_1 + \frac{1}{L_2} (\boldsymbol{\sigma}^T \mathbf{n}_2 - \boldsymbol{\sigma}_{i2}^T \mathbf{n}_2) \dot{\mathbf{u}}_2 = 0 \tag{6}$$

Eq. (6) can be further simplified using the definition of traction on the fracture planes, $\mathbf{t}_1^T = \boldsymbol{\sigma}_{i1}^T \mathbf{n}_1$ and $\mathbf{t}_2^T = \boldsymbol{\sigma}_{i2}^T \mathbf{n}_2$ as:

$$(\boldsymbol{\sigma}^T - \boldsymbol{\sigma}_o^T) \dot{\boldsymbol{\varepsilon}}_o + \frac{1}{L_1} (\boldsymbol{\sigma}^T \mathbf{n}_1 - \mathbf{t}_1^T) \dot{\mathbf{u}}_1 + \frac{1}{L_2} (\boldsymbol{\sigma}^T \mathbf{n}_2 - \mathbf{t}_2^T) \dot{\mathbf{u}}_2 = 0 \tag{7}$$

To satisfy Eq. (7) for any arbitrary values of $\dot{\boldsymbol{\varepsilon}}_o$, $\dot{\mathbf{u}}_1$ and $\dot{\mathbf{u}}_2$, the following conditions need to be met:

$$\begin{cases} \boldsymbol{\sigma} = \boldsymbol{\sigma}_o = \mathbf{a}_o \boldsymbol{\varepsilon}_o \\ \mathbf{n}_1^T \boldsymbol{\sigma} = \mathbf{t}_1 \\ \mathbf{n}_2^T \boldsymbol{\sigma} = \mathbf{t}_2 \end{cases} \tag{8}$$

The relationship between traction rates and displacement jump rates takes the following form:

$$\begin{cases} \dot{\mathbf{t}}_1 = \mathbf{K}_1^t \dot{\mathbf{u}}_1 \\ \dot{\mathbf{t}}_2 = \mathbf{K}_2^t \dot{\mathbf{u}}_2 \end{cases} \tag{9}$$

where $\mathbf{K}_1^t$, $\mathbf{K}_2^t$ are the tangent stiffness matrix of fracture planes 1 and 2 in the global coordinate system, respectively.

Substituting Eq. (9) into the rate form of Eqs. (8)$_2$, (8)$_3$ and using the incremental form of Eq. (8)$_1$, we have:

$$\begin{cases} \mathbf{n}_1^T \mathbf{a}_o \dot{\boldsymbol{\varepsilon}}_o = \mathbf{K}_1^t \dot{\mathbf{u}}_1 \\ \mathbf{n}_2^T \mathbf{a}_o \dot{\boldsymbol{\varepsilon}}_o = \mathbf{K}_2^t \dot{\mathbf{u}}_2 \end{cases} \tag{10}$$

Substitution of Eq. (4) into Eq. (10), along with some transformations

and arrangements, leads to:

$$\begin{cases} \left(\frac{1}{L_1} \mathbf{n}_1^T \mathbf{a}_o \mathbf{n}_1 + \mathbf{K}_1^t \right) \dot{\mathbf{u}}_1 + \frac{1}{L_2} \mathbf{n}_1^T \mathbf{a}_o \mathbf{n}_2 \dot{\mathbf{u}}_2 = \mathbf{n}_1^T \mathbf{a}_o \dot{\boldsymbol{\varepsilon}} \\ \frac{1}{L_1} \mathbf{n}_2^T \mathbf{a}_o \mathbf{n}_1 \dot{\mathbf{u}}_1 + \left(\frac{1}{L_2} \mathbf{n}_2^T \mathbf{a}_o \mathbf{n}_2 + \mathbf{K}_2^t \right) \dot{\mathbf{u}}_2 = \mathbf{n}_2^T \mathbf{a}_o \dot{\boldsymbol{\varepsilon}} \end{cases} \tag{11}$$

The equation can be transformed into a matrix format as:

$$\begin{bmatrix} \mathbf{M}_1 & \mathbf{M}_2 \\ \mathbf{M}_3 & \mathbf{M}_4 \end{bmatrix} \begin{bmatrix} \dot{\mathbf{u}}_1 \\ \dot{\mathbf{u}}_2 \end{bmatrix} = \begin{bmatrix} \mathbf{n}_1^T \mathbf{a}_o \\ \mathbf{n}_2^T \mathbf{a}_o \end{bmatrix} \dot{\boldsymbol{\varepsilon}} \tag{12}$$

where $\mathbf{M}_{i(i=1,4)}$ is 2-by-2 matrix for 2D case and 3-by-3 matrix for 3D case, respectively.

$$\mathbf{M}_1 = \frac{1}{L_1} \mathbf{n}_1^T \mathbf{a}_o \mathbf{n}_1 + \mathbf{K}_1^t ; \mathbf{M}_2 = \frac{1}{L_2} \mathbf{n}_1^T \mathbf{a}_o \mathbf{n}_2$$

$$\mathbf{M}_3 = \frac{1}{L_1} \mathbf{n}_2^T \mathbf{a}_o \mathbf{n}_1 ; \mathbf{M}_4 = \frac{1}{L_2} \mathbf{n}_2^T \mathbf{a}_o \mathbf{n}_2 + \mathbf{K}_2^t \tag{13}$$

From a given macro strain rate, one can calculate the velocity jumps of the two cracks:

$$\begin{bmatrix} \dot{\mathbf{u}}_1 \\ \dot{\mathbf{u}}_2 \end{bmatrix} = \begin{bmatrix} \mathbf{M}_1 & \mathbf{M}_2 \\ \mathbf{M}_3 & \mathbf{M}_4 \end{bmatrix}^{-1} \begin{bmatrix} \mathbf{n}_1^T \mathbf{a}_o \\ \mathbf{n}_2^T \mathbf{a}_o \end{bmatrix} \dot{\boldsymbol{\varepsilon}} = \begin{bmatrix} \mathbf{V}_1 \\ \mathbf{V}_2 \end{bmatrix} \dot{\boldsymbol{\varepsilon}} \tag{14}$$

where $\mathbf{V}_{i(i=1,2)}$ is 4-by-4 matrix for 2D case and 6-by-6 matrix for 3D case, respectively.

Using the rate form of Eq. (8)$_1$, Eqs. (4), (14) and conditions $f_1 \rightarrow 0$, $f_2 \rightarrow 0$, the macro stress–strain relationship is obtained as:

$$\dot{\boldsymbol{\sigma}} = \left[\mathbf{a}_o - \frac{1}{L_1} \mathbf{a}_o \mathbf{n}_1 \mathbf{V}_1 - \frac{1}{L_2} \mathbf{a}_o \mathbf{n}_2 \mathbf{V}_2 \right] \dot{\boldsymbol{\varepsilon}} \tag{15}$$

Eq. (15) shows an explicit link between the meso-scale responses (i.e., fracture planes 1 and 2) and the macro-scale behaviour. In other words, both the behaviour of the fracture planes and their surrounding bulk contribute to the overall behaviour of RVE (i.e., stress–strain relation at the constitutive level). Consequently, this relationship can be implemented within any continuum-based method, for example, the finite element method (FEM) or smoothed-particle hydrodynamics (SPH). More importantly, this relation features the characteristic lengths (i.e., L_1, L_2) of the considered RVE, and thus size-dependent behaviour is captured naturally without adding ad-hoc regulations.

2.2. A cohesive-frictional fatigue crack model

This section presents a completed cohesive-frictional fatigue model to describe the behaviour of the fracture planes. It is worth noting that subscript "c" is reserved in this research for all variables in the local coordinate system of the fracture planes. Therefore, these local variables should be transformed into the global coordinate system by a transformation matrix $\mathbf{R}$, where needed.

The displacement jumps between the two fracture surfaces, $\mathbf{u}_c$, can be decomposed into elastic ($\mathbf{u}^e$), plastic ($\mathbf{u}_c^p$) and fatigue ($\mathbf{u}_c^f$) components as follows:

$$\mathbf{u}_c = \mathbf{u}_c^e + \mathbf{u}_c^p + \mathbf{u}_c^f \tag{16}$$

The traction-displacement relationship is described as follows:

$$\mathbf{t}_c = \begin{bmatrix} t_n \\ t_{s1} \\ t_{s2} \end{bmatrix} = \begin{bmatrix} K_n[1-DH(t_n)] & 0 & 0 \\ 0 & K_s(1-D) & 0 \\ 0 & 0 & K_s(1-D) \end{bmatrix} \begin{bmatrix} u_n - u_n^p - u_n^f \\ u_{s1} - u_{s1}^p - u_{s1}^f \\ u_{s2} - u_{s2}^p - u_{s2}^f \end{bmatrix} \tag{17}$$

$$= \mathbf{K}_c^s(\mathbf{u}_c - \mathbf{u}_c^p - \mathbf{u}_c^f)$$

where $\mathbf{K}_c^s$ is the secant stiffness matrix of the cohesive fracture plane; K_n, K_s are the normal and shear cohesive elastic stiffness; t_n, t_{s1}, t_{s2} are the normal and shear tractions acting on the two surfaces of the fracture planes, respectively; D is the damage variable; u_n, u_{s1}, u_{s2} are the total normal and shear displacements; u_n^p, u_{s1}^p, u_{s2}^p, u_n^f, u_{s1}^f, u_{s2}^f, represent the plastic and fatigue normal, and shear displacements, respectively. The introduction of the Heaviside step function $H(t_n)$ implies that damage acts differently in tension and compression. In the tension regime, damage keeps developing upon the increase of cracking opening, while there is a partial stiffness recovery in compression due to the closing of cracks [14].

Next, the model is presented to calculate the growths of plastic and fatigue deformations of the fracture planes. In accomplishing this model, the following assumptions are adopted to facilitate the calculation of inelastic displacements and traction developments:

1. The strength of the material is represented by a bounding surface, which can shrink in the stress space under damage development. This shrinkage reflects the loss of material strength.
2. A subloading surface exists and is used to describe the fatigue damage evolution under cyclic loadings. This surface can move and contract simultaneously but is always below the bounding surface.
3. Depending on the distance between the current stress point and its image point, the softening modulus of materials changes along the stress trajectory.
4. To describe the plastic/fatigue flow and change of the softening modulus, the associated flow rules are used.

2.2.1. Bounding/yielding surface

The bounding surface takes the following standard equation of the hyperbola:

$$y(t_n, t_s, D) = \left(\frac{t_n - A}{B}\right)^2 - \left(\frac{t_s}{C}\right)^2 - 1 = 0 \tag{18}$$

where $t_s^2 = t_{s1}^2 + t_{s2}^2$, $A = (1-D)f_t^0 + B$, $B = C^0(1-D)/[2(1-D)+2D\mu^2]$, and $C = B\sqrt{(1-D)+D\mu^2}$, in which $\mu = \tan(\varphi)$ is the material internal friction coefficient (φ being the friction angle), and f_t^0 and C^0 are the tensile strength and initial cohesion of the material, respectively.

Upon the development of the damage variable, the bounding surface shrinks and finally becomes a straight line: $t_s \approx \pm\mu t_n$ when the material is almost damaged ($D \approx 1$). This linear relationship between the normal and shear tractions is the classical frictional Mohr-Coulomb criterion.

The damage variable D in Eq. (18) is the total damage considering the contribution of two components, the static damage variable (D_s) induced by static or quasi-static loads and the fatigue damage variable (D_f) induced by cyclic loads. As the stress state is on the bounding surface, there is a growth of static damage increment ($\dot{D}_s$). Meanwhile, the fatigue damage increment ($\dot{D}_f$) evolves if the subloading/fatigue criterion is met. Therefore, the total damage variable should be expressed as the sum of both damage increments:

$$D = \sum \left(\dot{D}_s + \dot{D}_f\right) \tag{19}$$

where $\dot{D}_s$ and $\dot{D}_f$ are not concurrent and defined later.

The associated flow rules are used in this study to describe plastic deformation on the fracture planes and are defined as:

$$\dot{u}_n^p = \dot{\lambda}\frac{\partial y}{\partial t_n}; \dot{u}_s^p = \dot{\lambda}\frac{\partial y}{\partial t_s} \tag{20}$$

where $\dot{\lambda}$ is the plastic multiplier, and derived by using the consistency condition $\dot{y} = 0$:

$$\dot{\lambda} = \frac{-\frac{\partial y}{\partial t_c}\frac{\partial t_c}{\partial \mathbf{u}_c}\dot{\mathbf{u}}_c}{\frac{\partial y}{\partial t_c}\frac{\partial t_c}{\partial \mathbf{u}_c^p}\frac{\partial t_c}{\partial t_c} + \frac{\partial y}{\partial t_c}\frac{\partial t_c}{\partial D}P + \frac{\partial y}{\partial D}P} = \frac{-\frac{\partial y}{\partial t_c}\frac{\partial t_c}{\partial \mathbf{u}_c}\dot{\mathbf{u}}_c}{S_B} \tag{21}$$

where P is defined in Section 3.2, and S_B is referred to as the plastic softening modulus on the bounding surface.

In this work, the coupling between static and fatigue damages is considered in the following form:

$$\dot{D}_s = e^{-u_{ps}}\dot{u}_{ps}\left(1 - D_f\right) \text{ with } \dot{u}_{ps} = \frac{1}{\delta_s}\sqrt{\left(\alpha\dot{u}_n^p\right)^2 + \beta\left[\left(\dot{u}_{s1}^p\right)^2 + \left(\dot{u}_{s2}^p\right)^2\right]} \tag{22}$$

where $u_{ps} = \sum \dot{u}_{ps}$ is the accumulated plastic displacement; non-dimensional parameters α and β signify the contributions of normal, and shear plastic displacements to the damage evolution; δ_s is relative displacement only used to normalise $\dot{u}_{ps}$; hence, it is taken as 0.01 mm for all simulations in this work.

2.2.2. Subloading/fatigue surface

The subloading surface, describing the deformation process of stress reversal histories, is assumed to take a geometry similar to the bounding surface to facilitate its kinematic movements. Thus, the equation of the subloading surface takes the form of a standard hyperbola:

$$y_o(t_n, t_s, X_n) = \eta\left[\left(\frac{t_n - a - X_n}{b}\right)^2 - \left(\frac{t_s}{c}\right)^2 - 1\right] = 0 \tag{23}$$

where $a = (1-\psi)f_t^0 + b$, $b = C^0(1-\psi)/[2(1-\psi)+2\psi\mu^2]$, and $c = b\sqrt{(1-\psi)+\psi\mu^2}$, wherein parameter ψ determines the initial position of subloading surface in the stress space and evolves upon the damage development, X_n is the kinematic hardening parameter that controls the current position of subloading surface, and η is used to indicate the current loading surface, with $\eta = 1$ for the top subloading surface and $\eta = -1$ for the bottom subloading surface (Fig. 2a). As the stress point moves along the bottom subloading surface in the stress space, the introduction of $\eta = -1$ ensures that the angle between the traction increment vector and the fatigue displacement rate vector is acute, which is an essential condition for maintaining the non-negative value of the fatigue work (i.e., the dot product of these vectors).

In the stress space, the top and bottom subloading surfaces are separated by a distance of e_{do} such that the following condition holds:

$$\psi_t = \psi_b - e_{do} \quad (0 \leq \psi_t \leq 1; 0 \leq \psi_b \leq 1; 0 \leq e_{do} \leq 1) \tag{24}$$
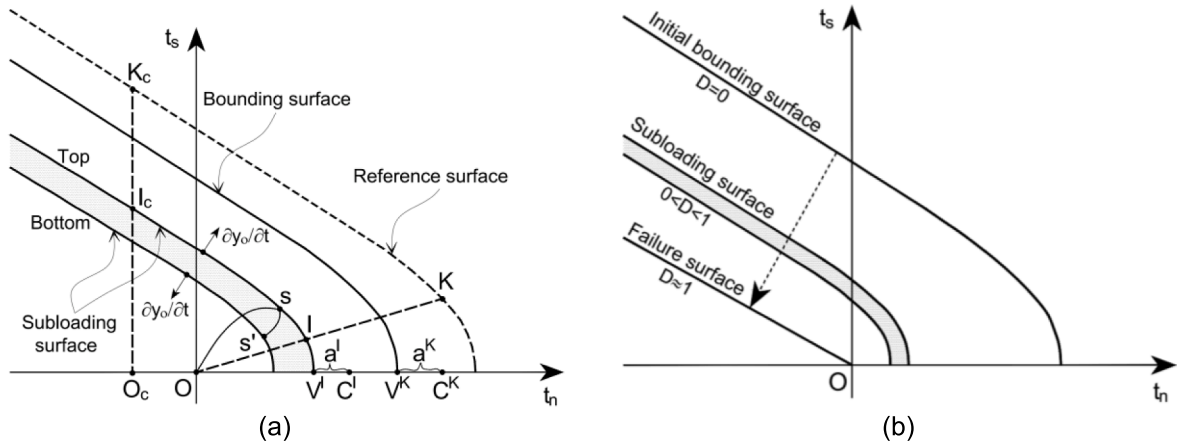
Fig. 2. (a) The vertices and centres of bounding and subloading surfaces in the stress space; (b) The shrinkage of the bounding surface and subloading surface upon damage evolution.

where subscripts "t" and "b" represent the top and bottom, respectively.

In this work, the initial top-subloading surface (y_0^t) is obtained by substituting the initial value of ψ_t (i.e., ψ_t^{ini}) into Eq. (23) and has a role as a fatigue threshold. This threshold is also used to detect the onset of crack and its orientation caused by cyclic loadings. As the stress state meets the fatigue criterion, fatigue crack/damage is activated. Otherwise, the material behaviour is always elastic. This assumption is reasonable since the effect of fatigue damage is neglectable when stress applied to the materials is small enough [6,49,61]. Besides, it is noted that as soon as the fatigue crack is activated, the bottom subloading surface will appear, creating a subdomain between the top and bottom subloading surfaces. This domain is called the elastic domain, and it decides the size of the subloading surface via the parameter e_{do} in Eq. (24), which is defined as:

$$e_{do} = e_{do}^0(1-D) \tag{25}$$

where e_{do}^0 is the initial value of the elastic domain, and any stress state belonging to the elastic domain behaves elastically.

From Eq. (25), the shrinkage of the elastic domain relies on the growth of the total damage variable D. This contraction reflects the dissipated fatigue process in materials. For the final damage stage of material, $D \approx 1$, the elastic domain is vanished, and thus the bounding and subloading surface coincides and becomes a straight line (Fig. 2b). Now, to gain a better understanding of how the subloading surface contributes to the deformation process of stress reversals, we can refer to stress paths OSS_1 and $S_1S_2S_3$ in Fig. 3. The stress path OS initially behaves elastically until it reaches point S located on the initial top

subloading surface, where fatigue crack/damage is activated. From this point onward, the behavior becomes elastoplastic for SS_1, which causes the subloading surface to translate and shrink as the stress point proceeds along its trajectory. However, when the stress path is reversed, the behaviour returns to elastic for S_1S_2, as it lies inside the subloading surface. As the stress point moves outside the subloading surface (along the stress path S_2S_3), the behaviour becomes elastoplastic again, resulting in movement and contraction of the subloading surface. These movements and contractions enable the model to simulate hysteretic behaviour, which will be further demonstrated in Sections 4 and 5.

The associated fatigue flow rule can now be proposed in a similar form to those in Eqs. (20) and (21), and takes the following form:

$$\dot{u}_n^f = \frac{-\frac{\partial y_0}{\partial t_c}\frac{\partial t_c}{\partial u_c}\dot{u}_c}{S_I}\frac{\partial y_0}{\partial t_n}; \dot{u}_s^f = \frac{-\frac{\partial y_0}{\partial t_c}\frac{\partial t_c}{\partial u_c}\dot{u}_c}{S_I}\frac{\partial y_0}{\partial t_s} \tag{26}$$

where S_I is the fatigue softening moduli, which can be obtained by imposing an interpolation rule that relates the value of S_I to the plastic softening modulus S_K and the distance between the current stress point I (or I_c) and the reference surface (Fig. 2a). For tension-shear and compression-shear domains, the value of S_I can be defined as follows, respectively:
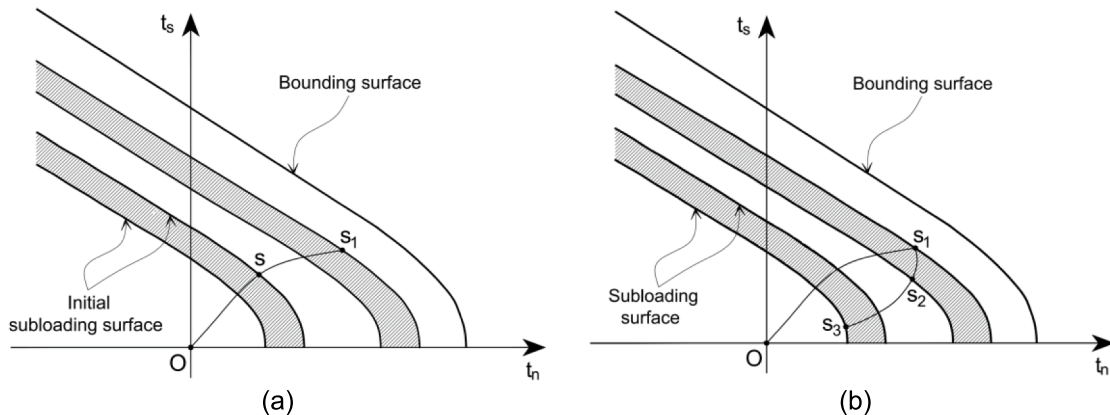

Fig. 3. Illustration of different stress paths in the normal-shear stress space: (a) Stress loading; (b) Stress reversal.

$$S_I = \begin{cases} \dfrac{S_K}{e^{-\frac{IK}{OK}Q}\left(1-\dfrac{IK}{OK}\right)^\kappa}, t_n \geq 0 \\[4mm] \dfrac{S_K}{e^{-\frac{I_cK_c}{O_cK_c}Q}\left(1-\dfrac{I_cK_c}{O_cK_c}\right)^\kappa}, t_n < 0 \end{cases} \quad (27)$$

where Q and κ are parameters controlling the magnitude of S_I; S_K is the plastic softening modulus evaluated at the image point on the reference surface (Fig. 2a), and can be determined following a similar process to obtain S_B in Eq. (21). The reference surface is defined as in Eq. (18), with the total damage D being replaced by the static damage D_s.

The proposed interpolation rule is based on the mechanism that the more the stress level, the more inelastic deformation occurs. This rule is represented by the distance between the stress point on the subloading surface and its image of the reference surface and enhanced by parameters Q and κ in Eq. (27). The proposed interpolation rule is unique because, referring to Fig. 2a, the current stress point is at I and its corresponding image point is at K, defined as the intersection beteen the line OI and the reference surface. As the stress point I approaches point K (i.e. $IK \to 0$), the subloading surface approaches the reference surface and thus S_I becomes S_K (i.e., $S_I \to S_K$) on the reference surface. The same observation applied to the stress point I_c on the compression space, except that O_cI_c is defined as the vertical line perpendicular to the normal-traction axis. In the tension-shear domain associated with the opening crack (Fig. 4a), fatigue damage is caused by both normal and shear tractions. Thus, it is reasonable to use the ratio of IK/OK to determine the fatigue flow rule. However, in the compression-shear regime where cracks tend to close, resulting in stiffness recovery of materials (Fig. 4b), shear traction mainly contributes to the development of fatigue-induced damage. Therefore, the ratio I_cK_c/O_cK_c is used since it can reflect the effect of shearing traction on fatigue damage. Nevertheless, if the stress point moves further to the left-hand side in the compression domain (Fig. 2a), the distance between the subloading surface and the reference surface is larger. As a result, the influence of shearing traction on fatigue growth becomes smaller. This less effect is satisfactory from a physical point of view that it is tough to shear cracks under high compression. In addition, the proposed interpolation rule shows the smooth transition when the stress point moves from the tension-shear domain to the compression-shear counterpart, which is indicated in Section 4.2.4.

To describe the fatigue-induced damage development under fatigue loadings, the incremental fatigue damage variable is taken as:

$$\dot{D}_f = h(D)\dot{u}_{pf} \text{ with } \dot{u}_{pf} = \frac{1}{\delta_f}\sqrt{\left(\alpha \dot{u}_n^f\right)^2 + \beta\left[\left(\dot{u}_{s1}^f\right)^2 + \left(\dot{u}_{s2}^f\right)^2\right]} \quad (28)$$

where δ_f is the relative displacement used to normalise $\dot{u}_{pf}$; the competition factor $h(D)$ represents the competitive mechanism during the three distinct processes of fatigue damage evolution [37,55], and takes the following form:

$$h(D) = \min(e^{-m_1 D} + e^{-m_2(1-D)}, 1) \quad (29)$$

where m_1 and m_2 are material parameters. The terms $e^{-m_1 D}$ and $e^{-m_2(1-D)}$ represent the decrease and increase of the fatigue damage rate during the cyclic loading process, respectively.

In addition to the fatigue flow and fatigue damage rules, the kinematics of the subloading surface is also a crucial component of the proposed model. This rule is established and presented in detail in Appendix A.

The above cohesive-frictional fatigue crack model can now be incorporated in the double-scale framework presented in Section 2.1 and implemented in any numerical method to simulate boundary value applications, which will be demonstrated in subsequent sections.

3. The model implementation

3.1. Crack initiation and its orientation

Cracking is one of the forms of localised failures in materials. The initiation and orientation of localisation bands have become an interesting topic for the scientific community over several decades. Rudnicki and Rice [57] were pioneers in using the acoustic tensor for detecting the onset and orientation of the localisation bands. This criterion was then used in many studies with reasonable results [13,47,48,52]. However, the approach relies on the specific hardening and/or flow rules employed in the classical continuum models [40,53]. Alternatively, the onset of the crack in quasi-brittle materials (such as rock or concrete) and its orientation can be determined by the maximisation of the detecting function as it reaches a critical value [31,32,62,70]. Specifically, the crack onset is identified when the tractions on a critical plane maximise the initial yield function (y_s) while ensuring that the function value remains non-negative $(\max_{\forall \theta}\{y_s(t_n, t_s) \geq 0\})$. In these studies, a scanning technique is employed to locate the critical plane, where the orientation angle θ of the plane is incrementally varied from $0°$ to $180°$. Although this scanning approach simplifies implementation,
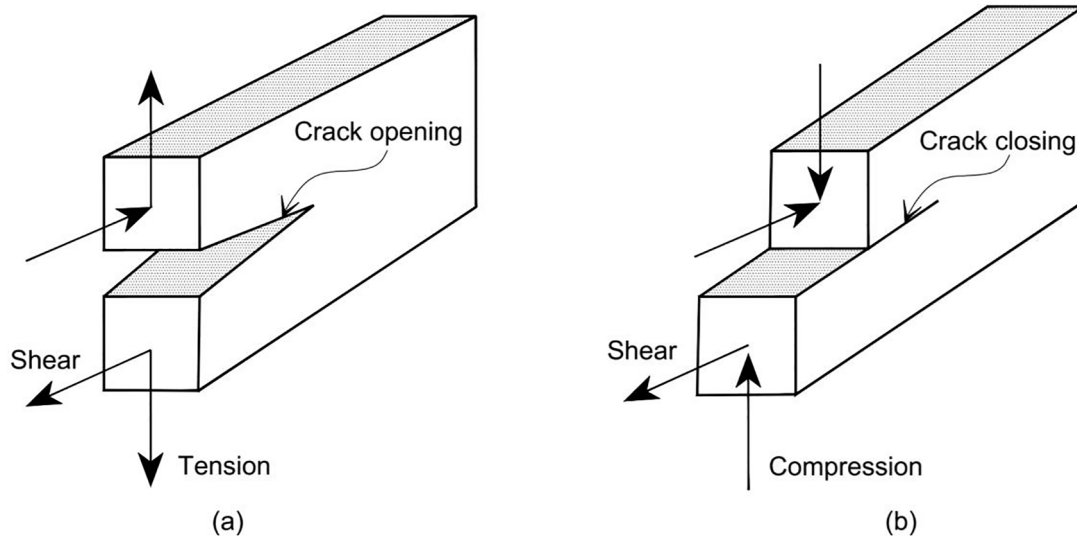

Fig. 4. (a) Tension-shear failure in the material; (b) Compression-shear failures in the material.

it requires significant computational resources as the orientation needs to be scanned at each simulation step. This research presents an analytical solution to replace the scanning approach for determining crack orientation.

Considering the top subloading surface in Eq. (23), for simplicity, Eq. (23) can be rewritten as:

$$y_0^t = t_s^2 - \frac{c^2}{b^2}(t_n - a - X_n)^2 + c^2 = 0 \tag{30}$$

The subloading surface y_0^t is a function of tractions, whose magnitudes change with θ. Thus, the extreme value of y_0^t can be achieved from the following equation:

$$y_0^{t'} = 2t_s \frac{dt_s}{d\theta} - \frac{2c^2}{b^2}(t_n - a - X_n)\frac{dt_n}{d\theta} = 0 \tag{31}$$

where $y_0^{t'}$ is the derivative of y_0^t with respect to θ.

The traction t_n and t_s in Eq. (31) can be related to macro stresses acting on the considered element shown in Fig. 5. The traction on any plane, featuring the normal vector **n** which forms an angle θ with the horizontal axis, is presented as follows:

$$\begin{bmatrix} t_n \\ t_s \end{bmatrix} = \mathbf{R}\mathbf{n}^T\boldsymbol{\sigma} = \begin{bmatrix} n_1 & n_2 \\ -n_2 & n_1 \end{bmatrix}\begin{bmatrix} n_1 & 0 \\ 0 & n_2 \\ n_2 & n_1 \end{bmatrix}^T\begin{bmatrix} \sigma_{xx} \\ \sigma_{yy} \\ \sigma_{xy} \end{bmatrix} \tag{32}$$

where n_1 and n_2 are unit vectors of **n** in the global coordinate system.

Using the basic trigonometry, Eq. (32) can be expressed explicitly as:

$$\begin{bmatrix} t_n \\ t_s \end{bmatrix} = \begin{bmatrix} \frac{1}{2}(\sigma_{xx} - \sigma_{yy})\cos2\theta + \sigma_{xy}\sin2\theta + \frac{1}{2}(\sigma_{xx} + \sigma_{yy}) \\ \frac{1}{2}(-\sigma_{xx} + \sigma_{yy})\sin2\theta + \sigma_{xy}\cos2\theta \end{bmatrix} \tag{33}$$

Taking derivatives on both sides of Eq. (33) with respect to θ, one has:

$$\begin{bmatrix} \frac{dt_n}{d\theta} \\ \frac{dt_s}{d\theta} \end{bmatrix} = \begin{bmatrix} (-\sigma_{xx} + \sigma_{yy})\sin2\theta + 2\sigma_{xy}\cos2\theta \\ (-\sigma_{xx} + \sigma_{yy})\cos2\theta - 2\sigma_{xy}\sin2\theta \end{bmatrix} \tag{34}$$

From Eq. (33), Eq. (34) and Eq. (31), the following equation can be obtained:

$$\begin{bmatrix} \frac{dt_n}{d\theta} = 0 \\ \frac{dt_s}{d\theta} - \frac{2c^2}{b^2}(t_n - a - X_n) = 0 \end{bmatrix} \tag{35}$$
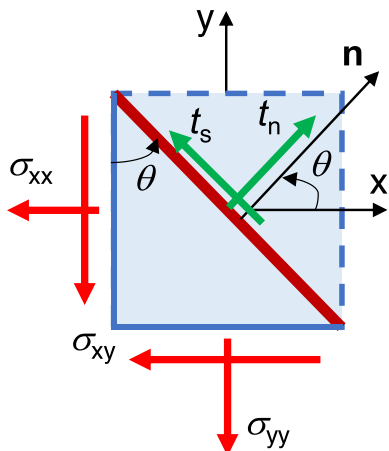

Fig. 5. An element subjected to stress state in plane strain/stress.

Substituting Eq. (33) and Eq. (34) into Eq. (35) gives:

$$\begin{bmatrix} (-\sigma_{xx} + \sigma_{yy})\sin2\theta + 2\sigma_{xy}\cos2\theta = 0 \\ a_1\cos2\theta + a_2\sin2\theta = a_3 \end{bmatrix} \tag{36}$$

where $a_1 = \left(\frac{c^2}{b^2} + 1\right)(-\sigma_{xx} + \sigma_{yy})$, $a_2 = \left(-\frac{2c^2}{b^2} - 2\right)\sigma_{xy}$, $a_3 = \frac{c^2}{b^2}(-2a - 2X_n + \sigma_{xx} + \sigma_{yy})$

The solutions of Eq. (36), detailed in Appendix, give the extrema values for function y_0^t, and the onset of crack is detected if this condition is satisfied ($\max_{\forall\theta}\{y_0^t(t_n, t_s) \geq 0\}$). The corresponding critical angle θ_{cr} represents the crack orientation. To demonstrate the correctness of the analytical solution in detecting crack orientation, a 2D element experiencing a specific stress state is examined. The stress state is defined as $[\sigma_{xx}\ \sigma_{yy}\ \sigma_{xy}] = [2\ 5\ 1]$ (MPa). The model parameters employed in Eq. (23) consist of $f_t^0 = 3.6$ MPa, $C^0 = 10$ MPa, $\mu = 0.84$, and ψ_t^{ini} and X_n set to 0. Fig. 6 presents the value of y_0^t and its derivative ($y_0^{t'}$) for all possible scanning θ values, ranging from 0 to 180°, and are represented by the solid-dot lines. On the other hand, our analytical solutions from Eq. (36) results in two stationary points (cross-points) in Fig. 6a, while the value of y_0^t corresponding to these stationary points are presented in Fig. 6b. Both approaches (i.e., scanning and analytical) detected the onset of the crack at the critical angle of $\theta_{cr} = 73.2°$. This suggests that our analytical solution can accurately detect the onset and orientation of cracks without scanning, thus saving significant computational costs. Further discussion on the computational efficiency associated with our proposed technique will be discussed in Section 5.1.2.1.

3.2. Traction return algorithm for the cohesive fatigue model

During crack inception and propagation, the cohesive fatigue model governs the behaviour of cracks. Therefore, it is necessary to have an appropriate stress return algorithm for the cohesive model to accurately update tractions on cracks based on displacement jumps. In this study, the semi-implicit traction algorithm is employed due to its computational efficiency and accuracy [10,33,48]. The algorithm begins with the calculation of $\mathbf{t}_c^{tr}$ on the fracture plane from an incremental local displacement jumps $\dot{\mathbf{u}}_c$ using Eq. (17). Based on $\mathbf{t}_c^{tr}$, the trial bounding function (y^{tr}) and trial subloading function (y_0^{tr}) are then calculated using Eqs. (18) and (23), respectively. In the case with $y^{tr} \geq 0$, the Taylor expansion of the bounding function yields:

$$y = y^{tr} + \frac{\partial y^T}{\partial \mathbf{t}_c}\frac{\partial \mathbf{t}_c}{\partial \mathbf{u}_c^p}\dot{\mathbf{u}}^p + \frac{\partial y^T}{\partial \mathbf{t}_c}\frac{\partial \mathbf{t}_c}{\partial D}\dot{D} + \frac{\partial y}{\partial D}\dot{D} = 0 \tag{37}$$

Using Eqs. (19), (20) and (22), $\dot{D}$ in Eq. (37) is connected to $\dot{\lambda}$ as follows:

$$\dot{D} = \dot{D}_s = e^{-u_{ps}}\dot{u}_{ps}(1 - D_f) = \frac{e^{-u_{ps}}}{\delta_s}(1 - D_f)\sqrt{\left(\alpha\frac{\partial y}{\partial t_n}\right)^2 + \left(\beta\frac{\partial y}{\partial t_s}\right)^2}\dot{\lambda} = P\dot{\lambda} \tag{38}$$

Eqs. (20), (38) are substituted into Eq. (37), and the scalar $\dot{\lambda}$ is found to be:

$$\dot{\lambda} = \frac{-y^{tr}}{\frac{\partial y^T}{\partial \mathbf{t}_c}\frac{\partial \mathbf{t}_c}{\partial \mathbf{u}_c^p}\frac{\partial y}{\partial \mathbf{t}_c} + \frac{\partial y^T}{\partial \mathbf{t}_c}\frac{\partial \mathbf{t}_c}{\partial D}P + \frac{\partial y}{\partial D}P} \tag{39}$$

After computing increments of internal variables based on Eqs. (20), (22), the corrected traction is updated as:

$$\mathbf{t}_c = \mathbf{t}_c^{tr} + \frac{\partial \mathbf{t}_c}{\partial \mathbf{u}_c^p}\dot{\mathbf{u}}^p + \frac{\partial \mathbf{t}_c}{\partial D}\dot{D}_s \tag{40}$$

When the stress state is on the subloading surface, a similar procedure to that used for the bounding surface is employed to determine internal variables and update the traction. However, before the determination of internal variables, it is necessary to compute the pair values
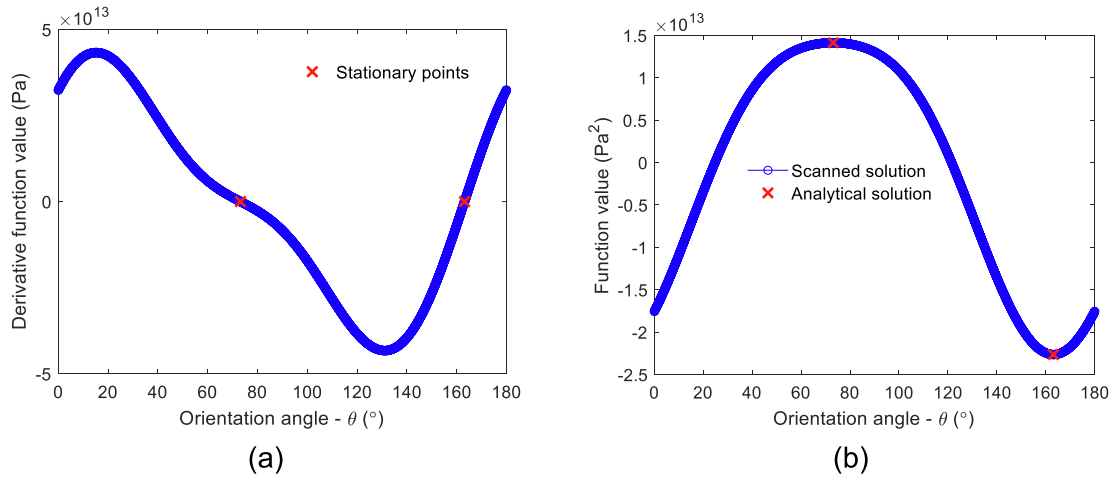
Fig. 6. Comparison between the solution of scanning technique and analytical solution: (a) Stationary points; (b) Maximum and minimum value of the top sub-loading surface.

of (IK, OK) or (I_cK_c, O_cK_c) in Eq. (27). After tractions are updated based on the values of (IK, OK) or (I_cK_c, O_cK_c) and other internal variables, the kinematic hardening X_n is then updated. Algorithm 1 illustrates the completed traction return algorithm for the proposed fatigue cohesive-frictional model.

3.3. Stress return algorithm of the double-scale model

Once the fracture initiates and fracture planes are formed, the post-localised behaviour of the material RVE will be rather complicated with two distinct responses for the outside and on the planes. These notice-able responses interact with each other through the traction continuity across the fracture planes. Therefore, there needs to be a proper algo-rithm to describe this interaction and track the evolution of the macro behaviour of the material RVE. Due to the simplification of the algo-rithm for the model featuring one crack, this section will only present the algorithm for two cracks with two orientations $\mathbf{n}_1$ and $\mathbf{n}_2$ have been triggered. However, the one-crack algorithm is similar to the two-crack algorithm, except that the components related to the two cracks are neglected. Adopting the implicit algorithm proposed by [31,42,48] to update stress based on a given total strain increment, the algorithm begins with the calculation of displacement jumps with the assumption of elastic behaviour on the fracture planes, shown in Algorithm 2. Stresses and tractions are then calculated based on these jumps. Nevertheless, an iterative process is required to correct the current stresses and tractions to ensure traction continuity across the fracture planes. To do this, two vectors of residual traction corresponding to two cracks are defined:

$$\mathbf{r}_1 = \mathbf{n}_1^T\boldsymbol{\sigma} - \mathbf{t}_1 \text{ and } \mathbf{r}_2 = \mathbf{n}_2^T\boldsymbol{\sigma} - \mathbf{t}_2 \tag{41}$$

where $\mathbf{t}_1 = \mathbf{R}_1^T\mathbf{t}_{c1}$, $\mathbf{t}_2 = \mathbf{R}_2^T\mathbf{t}_{c2}$

The first-order Taylor expansion of the residual traction at the new state can be written as:

$$\mathbf{r}_1^{new} = \mathbf{r}_1^{old} + \mathbf{n}_1^T\delta\boldsymbol{\sigma} - \delta\mathbf{t}_1 \text{ and } \mathbf{r}_2^{new} = \mathbf{r}_2^{old} + \mathbf{n}_2^T\delta\boldsymbol{\sigma} - \delta\mathbf{t}_2 \tag{42}$$

where $\delta\boldsymbol{\sigma}$, $\delta\mathbf{t}_1$ and $\delta\mathbf{t}_2$ are the iterative stress and global tractions at the new state, which is calculated as follows:

$$\delta\boldsymbol{\sigma} = -\frac{1}{L_1}\mathbf{a}_o\mathbf{n}_1\delta\mathbf{u}_1 - \frac{1}{L_2}\mathbf{a}_o\mathbf{n}_2\delta\mathbf{u}_2 \tag{43}$$

$$\delta\mathbf{t}_1 = \mathbf{K}_1^t\delta\mathbf{u}_1 \text{ and } \delta\mathbf{t}_2 = \mathbf{K}_2^t\delta\mathbf{u}_2 \tag{44}$$

It should be noted that the strain increment $\Delta\boldsymbol{\varepsilon}$ is omitted in Eq. (43) as it is already used in the trial step before performing the iterative

procedure. Enforcing the requirement $\mathbf{r}_1^{new} = 0$, $\mathbf{r}_2^{new} = 0$ and substituting Eqs. (43), (44) into Eq. (42), the iterative displacement increments $\delta\mathbf{u}_1$ and $\delta\mathbf{u}_2$ are calculated as:

$$\begin{bmatrix} \delta\mathbf{u}_1 \\ \delta\mathbf{u}_2 \end{bmatrix} = \begin{bmatrix} \mathbf{M}_1 & \mathbf{M}_2 \\ \mathbf{M}_3 & \mathbf{M}_4 \end{bmatrix}^{-1} \begin{bmatrix} \mathbf{r}_1^{old} \\ \mathbf{r}_2^{old} \end{bmatrix} \tag{45}$$

Once $\delta\mathbf{u}_1$ and $\delta\mathbf{u}_2$ have been determined, these are transformed back to the local coordinate system to update local tractions following Al-gorithm 1. The iterative stress is then computed based on Eq. (43). The procedure described above is then repeated until a convergence crite-rion is satisfied:

$$\frac{\|\mathbf{r}_k\|}{\|\mathbf{t}_k\|} < \text{tolerance (tol)} \tag{46}$$

The whole implicit algorithm for stress update is presented in Al-gorithm 2. Eventually, Algorithm 1, Algorithm 2 and Flow Chart 1 complete the framework of the double-scale approach with two-embedded fracture planes.

3.4. Cycle jump technique

In high-cycle fatigue problems, a cycle-by-cycle simulation involves a substantial computational cost. Therefore, a cycle jump technique related to constantly repeated loads [64,65] is employed in this work. With this method, the simulation can leap from the first load cycle to the last load cycle of a set if the damage development is stable in that set of loading cycles. The damage degradation of those loading cycles is then decided by the extrapolation approach [35,38,56,67]. Specifically, the damage after $N_{i+\Delta N_i}$ cycles is extrapolated from the damage after N_i cycles. If the damage evolution of an integration point j as a function of the number of cycles is known, the gradient of this function (dD/dN) can be written as follows:

$$\frac{dD_i^j}{dN} \approx \frac{\Delta D^j}{\Delta N_i} \tag{47}$$

The number of cycles ΔN_i that can be jumped is then determined using the following equation [64]:

$$\Delta N_i = \frac{\Delta D}{max_j\left\{\frac{dD_i^j}{dN}\right\}} \tag{48}$$

where ΔD is a pre-established value, $max_j\left\{\frac{dD_i^j}{dN}\right\}$ is the maximum gradient in all integration points. The values of ΔN_i vary with a specific
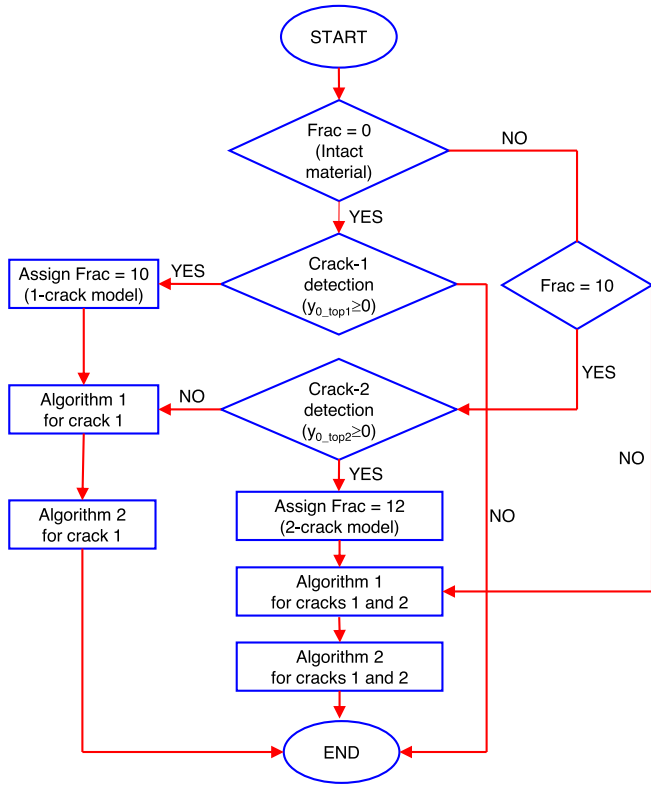
Flow Chart 1. Flow chart of an algorithm for double-scale approach.

number of cycles N_i owing to the change of gradient (dD/dN) throughout the fatigue process.

The damage rate with regard to the number of loading cycles N is computed to complete the cyclic jump approach as follows [22]:

$$\frac{dD}{dN} = C_{jump}\left(\frac{\Delta G}{G_c}\right)^{m_{jump}} \tag{49}$$

where C_{jump}, m_{jump} are calibration parameters; G_c is fracture energy, and $\Delta G = G^{max} - G^{min}$ is the rate of energy release at the integration point.

The energy release rates G^{max} and G^{min} for a cycle jump can be estimated using the trapezoidal rule, which corresponds to the area under the $\mathbf{t}_c$-$\mathbf{u}_c$ curve as follows:

$$G = \sum_{k=1}^{n}\left(\frac{\mathbf{t}_c^k + \mathbf{t}_c^{k+1}}{2}\right)\left(\dot{\mathbf{u}}_c^{k+1} - \dot{\mathbf{u}}_c^k\right) \tag{50}$$

where n is the total number of simulation steps with each cycle jump.

4. Parameter identification, model behaviour and validation at the constitutive level

4.1. Parameter identification of the constitutive model

This section focuses on identifying and calibrating the proposed model parameters to establish a clear connection between these parameters and their physical representations, and the material properties they represent. The proposed constitutive model requires three sets of parameters: material properties, elastoplastic parameters, and fatigue parameters. Material properties, including modulus E, Poisson's ratio ν, tensile strength f_t^0, and initial cohesion of the material C^0, can be determined through standard tests. For instance, the tensile strength f_t^0 can be obtained from uniaxial tension tests. Fig. 7(a) illustrates an example of determining tensile strength, with a value of 2.6 MPa, in a tension uniaxial test conducted on concrete [11]. Once f_t^0 is identified, C^0 is determined by fitting an experimental dataset of localisation onset (i.e., yielding points) with the initial position of the bounding/yielding surface in the normal-shear traction space. To determine the yielding points of the material, triaxial compression tests or direct shear tests need to be performed. For example, the direct shear test results are used to illustrate the calibration of C^0 [72]. Fig. 7(b) presents the initial bounding surface fitted to yielding points, using the parameter C^0 of 8 MPa. The internal friction angle φ for concrete, for example, can range from 37° to 57° [17].

Regarding elastoplastic parameters, the parameters K_n and K_s can be calibrated with the initial unloading and reloading slopes of the cyclic tests, as indicated in Section 4.3. The parameter α is associated with mode I fracture energy, and it can be fine-tuned until the area under the stress–strain curve produced by the model matches the one obtained from experiment, as depicted in Fig. 7(a). With a α value of 0.15, the predictive stress–strain curve reasonably agrees with the experimental result. A larger value of α leads to a higher rate of softening behaviour and smaller specific fracture energy. Similarly, the parameter β is strongly linked to mode II fracture energy observed in shear tests. The value of β is determined after α is known.

The final set of model parameters consists of fatigue parameters. The parameter δ_f determines the magnitude of fatigue damage increment, which has a significant impact on the fatigue lives of materials. The
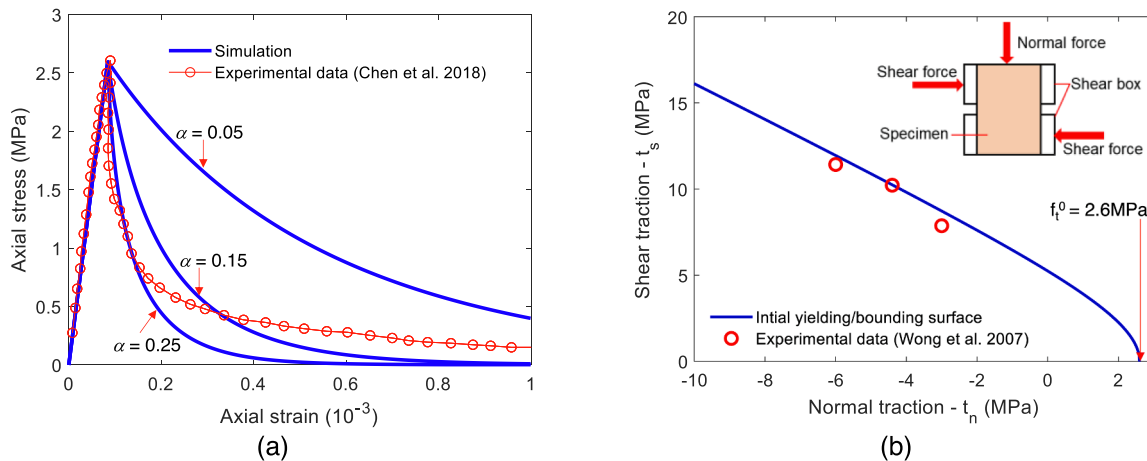

Fig. 7. Illustration of the calibration process for the model parameters: (a) Comparison between the proposed model's response and experimental data in the uniaxial tension test; (b) Yielding points obtained from direct shear tests and calibrated initial bounding/yielding surface achieved by the model.

parameters m_1 and m_2 are calibrated to capture the deformation development or modulus reduction observed in the initial and final stages of fatigue responses, respectively. Additionally, the values of Q and κ can be determined by conducting fatigue tests under different stress levels, as these parameters greatly influence the fatigue lives of materials, especially at low-stress levels. On the other hand, the values of ψ_t^{ini} and e_{do}^0 are chosen based on intuition. However, a parametric study examining the effect of fatigue parameters on constitutive behaviour will be presented in Section 4.2.2 to enhance the understanding of these parameters.

4.2. Illustration of model behaviour under different loading conditions

4.2.1. Model behaviour under pure tensile cyclic loading (Example 1)

In this section, an element test is conducted under different loading paths to illustrate the constitutive performance of the proposed model. This test is represented by a squared RVE with a length of 0.05 m. The material properties used in the test are Young's modulus $E = 33$ GPa, Poisson's ratio $\nu = 0.2$, initial cohesion $C^0 = 30$ MPa, tensile strength $f_t^0 = 4.5$ MPa. Elasto-plastic parameters of the model are: $\alpha = 0.6$, $\beta = 0.6$, $\mu = 0.5$, elastic stiffness $K_n = K_s = 2 \times 10^{12}$ Pa/m; fatigue parameters are: $\psi_t^{ini} = 0.55$, $e_{do}^0 = 0.15$, $\delta_f = 0.5 \times 10^{-3}$ (m), $m_1 = 1.0$, $m_2 = 1.0$, $Q = 0$. Two different loading conditions are applied to the RVE, shown in Fig. 8. Specifically, stage 1 is cyclic loading in the x-direction with a stress level from 2 MPa to 3 MPa until reaching the cycle number of 56, followed by a strain-controlled loading up to $\varepsilon_{xx} = 0.02$ %.

Fig. 9a illustrates the macro behaviour of RVE. The behaviour is firstly elastic until reaching point A, where the first crack appears. The crack appearance occurs when the stress point meets the top subloading surface. Subsequently, the stress point moves along with this surface, leading to the hardening behaviour (line AB). This hardening process is distinctive from our earlier works [31,33,62,70], where the behaviour at the constitutive level is always elastic before reaching the yield surface. Similarly, the meso behaviour of the crack in Fig. 9b experiences the firstly elastic stage, followed by the hardening phase. Meanwhile, the behaviour outside the crack is always elastic due to the assumption of intact bulk material as the fracture plane occurs. The RVE is then subjected to cyclic loading ranging from 2 MPa to 3 MPa until reaching the cycle number of 56. During this cyclic process, the proposed model can capture the hysteresis behaviour, indicated by differences in reloading and unloading paths shown in Fig. 9a and b. This ability is thanks to the introduction of the subloading surface which can translate into the normal-shear stress space. Fig. 9d clearly illustrates that the normal fatigue displacement increases under repeated loading, resulting in damage development. This development causes the contraction of the elastic domain (e_{do}). As a result, the distance between two consecutive hysteresis loops becomes larger, as shown in Fig. 9a and b. The wider loops and damage growth during fatigue loading indicate the dissipated energy of material under cyclic loading.

Based on the properties, model parameters and loading paths of RVE above (Example 1, Fig. 8), a parametric study is carried out to demonstrate the size-dependent behaviour of the material at the constitutive level. In this study, the length of RVE in the y-direction keeps the same, but the other length changes from 50 mm to 100 mm. Fig. 10a illustrates
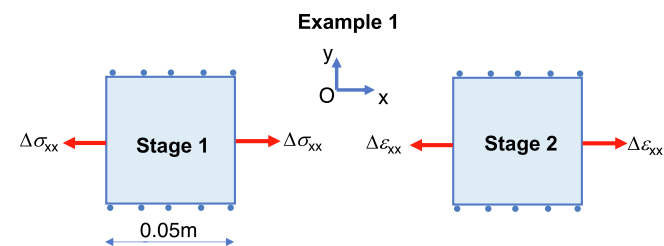
that stress–strain curves scale with the different specimen sizes; specifically, the behaviour of RVE is more brittle as the size increases. However, it can be seen in Fig. 10b that the relation between damage and the number of cycles on the fracture plane is invariant regardless of specimen lengths, showing the invariance of the dissipation rate.

4.2.2. The effect of fatigue parameters on the constitutive behaviour

To illustrate the influence of individual fatigue model parameters on the constitutive response, a parametric analysis using the same loading conditions and model parameters as the test presented in Section 4.2.1 is conducted in this section.

Fig. 11 provides valuable insights into the effects of various fatigue model parameters on the fatigue lives of the test. As shown in Fig. 11a, the value of δ_f has a significant impact on the fatigue lives, irrespective of different stress levels. As the value of δ_f increases, the fatigue lives also increase accordingly. On the other hand, the values of e_{do}^0 exhibit a notable effect on fatigue lives primarily at low stress levels (Fig. 11b). Similarly, larger values of κ and Q contribute significantly to a considerable increase in the number of cycles to failure, particularly at low stress levels, as depicted in Fig. 11c and d. In contrast, different values of m_1 and m_2 exhibit slight influence on the fatigue lives of the test (Fig. 11e and f).

4.2.3. Model behaviour under non-proportional loading conditions (Example 2)

To further demonstrate the general capability of the proposed model under complex loading conditions, non-proportional loading paths are examined in this section. An element test, shown in Fig. 12 with the same material properties and model parameters as the test in Section 4.2.1, is carried out. However, the RVE experiences a series of three different loading stages as follows. In the first stage, a cyclic stress amplitude ranging from 2 MPa to 3 MPa in the x-direction is applied until the number of cycles is 45. Then a strain-controlled loading in the same direction is conducted up to $\varepsilon_{xx} = 0.05$ %. Finally, the RVE undergoes a strain-controlled loading in the y-direction up to $\varepsilon_{yy} = 0.05$ %. It is noted that during loading in one direction, strain in the other direction is kept constant.

To illustrate a necessity of a secondary crack appearing and developing, the double-scale approach featuring one crack is used to show its drawback under complicated loading paths. Fig. 13 shows the stress–strain responses produced by the one-crack model, wherein the σ_{xx} increases linearly up to the point of the first crack appearance at the stress value of 2.25 MPa. The behaviour in direction x is then elastoplastic under cyclic loading up to the cycle of 45, while σ_{yy} varies from 0 to 0.85 MPa due to strain restraint in the y-direction and the Poisson effect, shown in Fig. 13b. At the end of stage 1, σ_{xx} is 2 MPa, while σ_{yy} is 0.5 MPa. In stage 2, σ_{xx} increases up to the peak of 3.4 MPa, and then experiences a softening phase which is controlled by the bounding surface. The peak is significantly smaller than the tensile strength of the material (i.e. 4.5 MPa) as the material gradually degrades during cyclic loading due to fatigue damage development. Meanwhile, a decrease in stress σ_{yy} to reach the value of 0.23 MPa can be seen. However, the stress σ_{yy} increases linearly during the third phase and even exceeds the tensile strength until reaching 17.3 MPa at the end of this stage. This unphysical phenomenon is called the stress-locking issue because the one-crack model only allows one crack to develop. Therefore, this model cannot deal with the change in loading paths where a secondary crack can be formed. One way to overcome this problem is to introduce the appearance and development of a secondary crack [31,32]. In contrast to these studies, which focus on monotonic loading, this paper examines cyclic loading.

Fig. 14a and b illustrate the stress–strain responses produced by the two-crack model. The behaviour observed in stages 1 and 2 is the same as that in the one-crack model analysis. However, in stage 3, the secondary crack occurs when the stress σ_{yy} reaches the value of 2.25 MPa,

Example 1

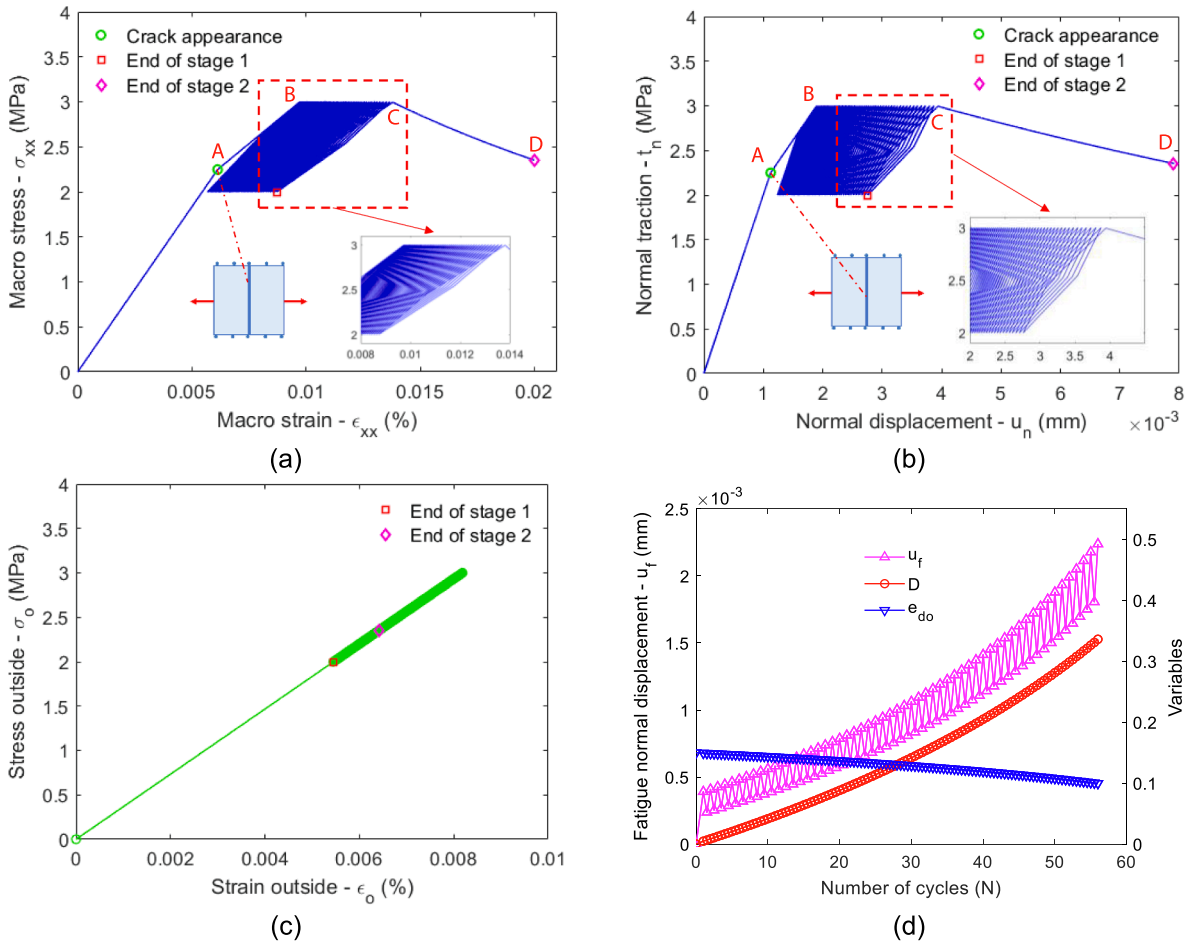**Fig. 8.** Pure tensile loading stages.

Fig. 9. The behaviour of the proposed model under tensile cyclic loading: (a) Macro stress–strain relationship; (b) Meso behaviour of the crack; (c) Stress–strain response outside the crack; (d) Evolution of internal variables describing crack behaviour.
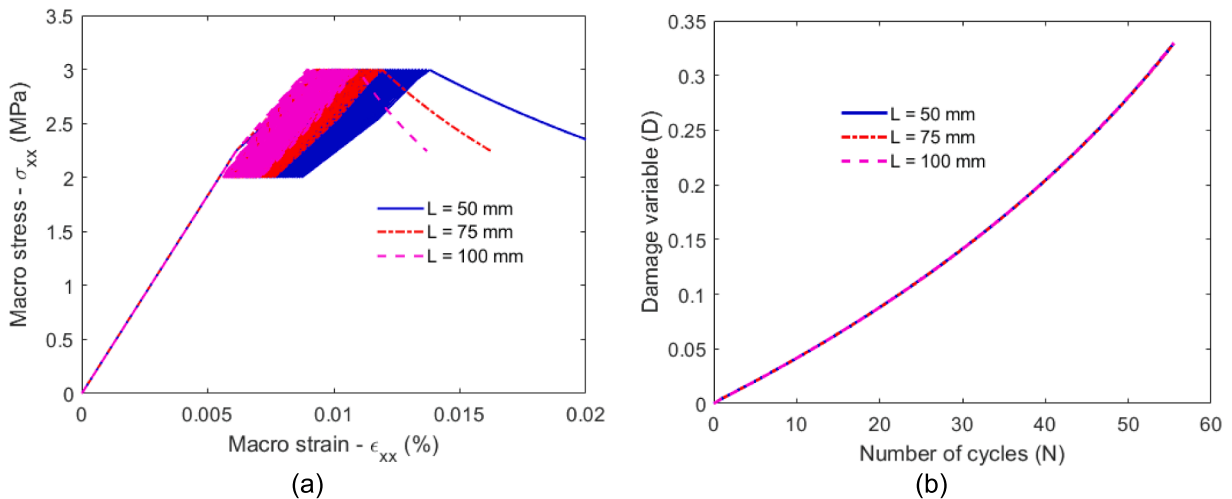

Fig. 10. Parametric study on size-dependent behaviour: (a) Stress–strain responses for different RVE lengths; (b) Damage versus the number of cycles on the fracture plane up to the same damage level ($D = 0.33$).

then the behaviour undergoes a hardening phase up to the peak of 4.44 MPa, which is slightly smaller than the tensile strength. This is because, during the hardening stage, the material experiences minor damage development as the stress point moves along the top subloading surface. After hitting the peak, the σ_{yy} undergoes the softening stage and finally reaches 1.25 MPa, while σ_{xx} also decreases to 0.59 MPa. The appearance

and development of the secondary crack help the proposed model overcome the stress-locking issue.

The evolution of behaviours on fracture planes is crucial to observe the connection between macro and meso behaviours and the mutual impact between these two planes. Therefore, the displacement-traction curves of both cracks are plotted in Fig. 14c and d to investigate this
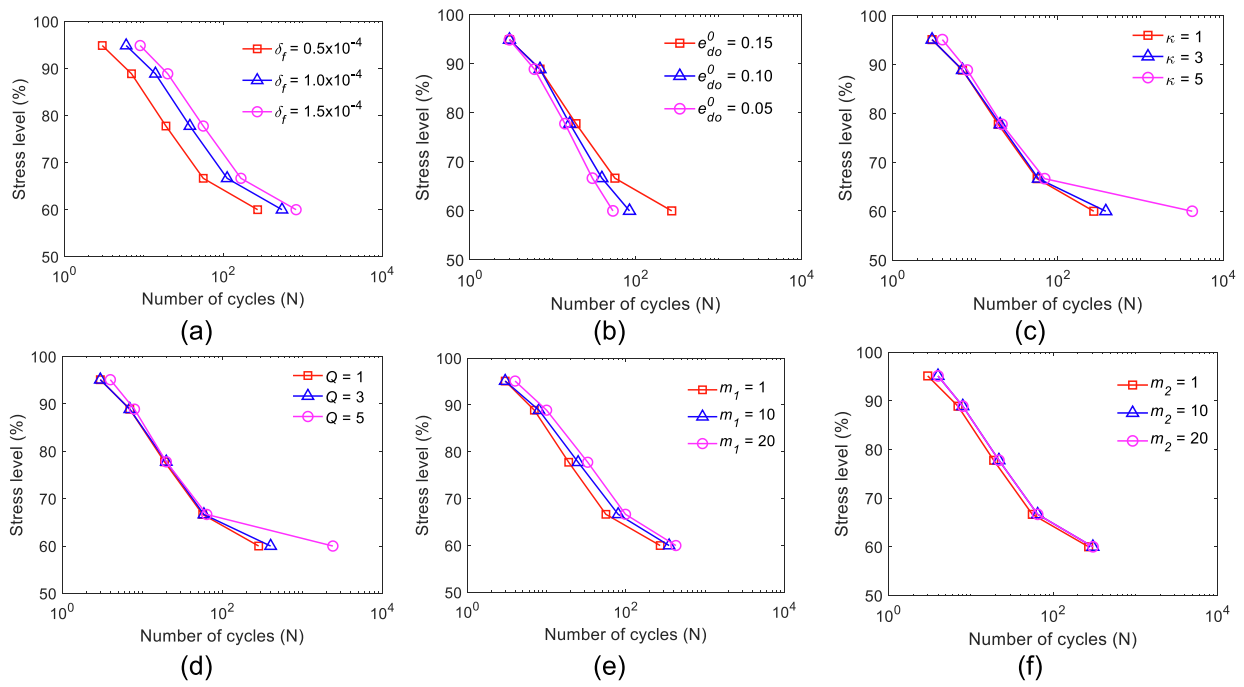
Fig. 11. Influences of fatigue parameters on fatigue lives of the tension cyclic tests: (a) Effect of δ_f; (b) Effect of e_{do}^0; (c) Effect of κ; (d) Effect of Q; (e) Effect of m_1; (f) Effect of m_2. It is important to note that the stress level in this example is defined as the ratio between the maximum applied stress and the tensile strength.
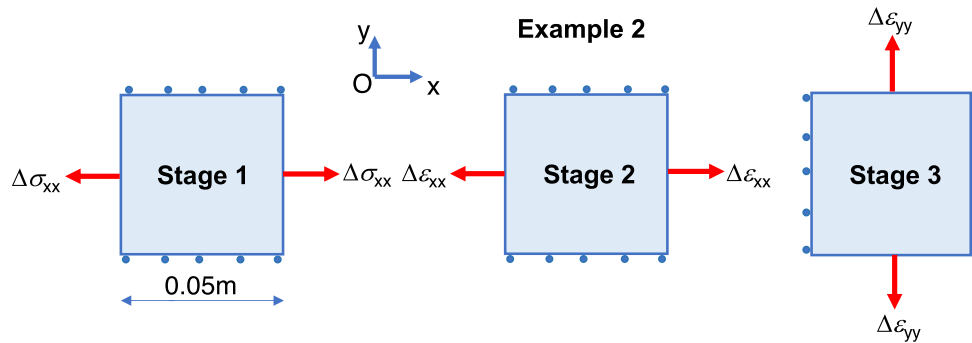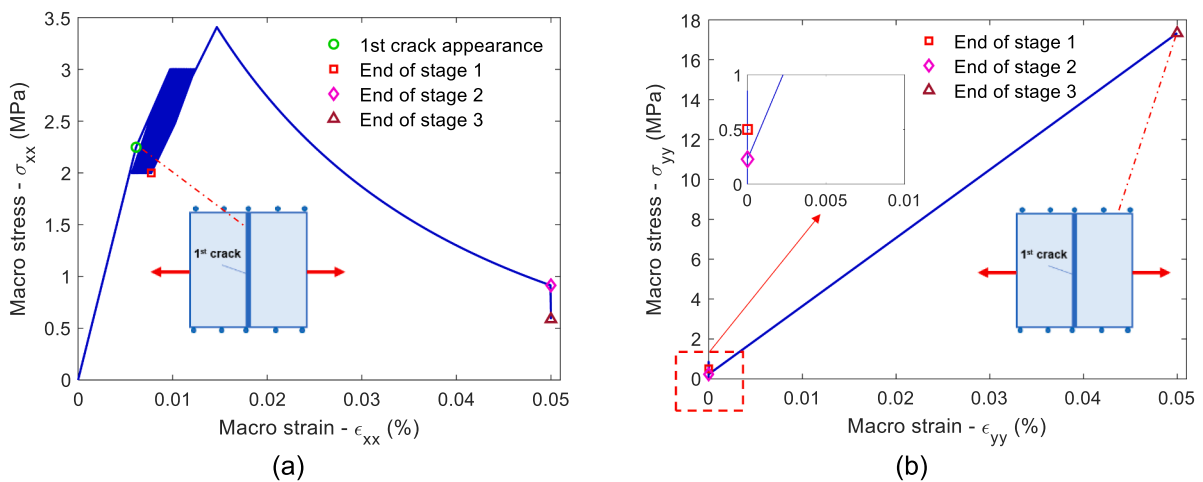

Fig. 12. Non-proportional loading stages.

Fig. 13. The behaviour of the one-crack model: (a) Stress–strain curve in the x-direction; (b) Stress–strain curve in the y-direction.
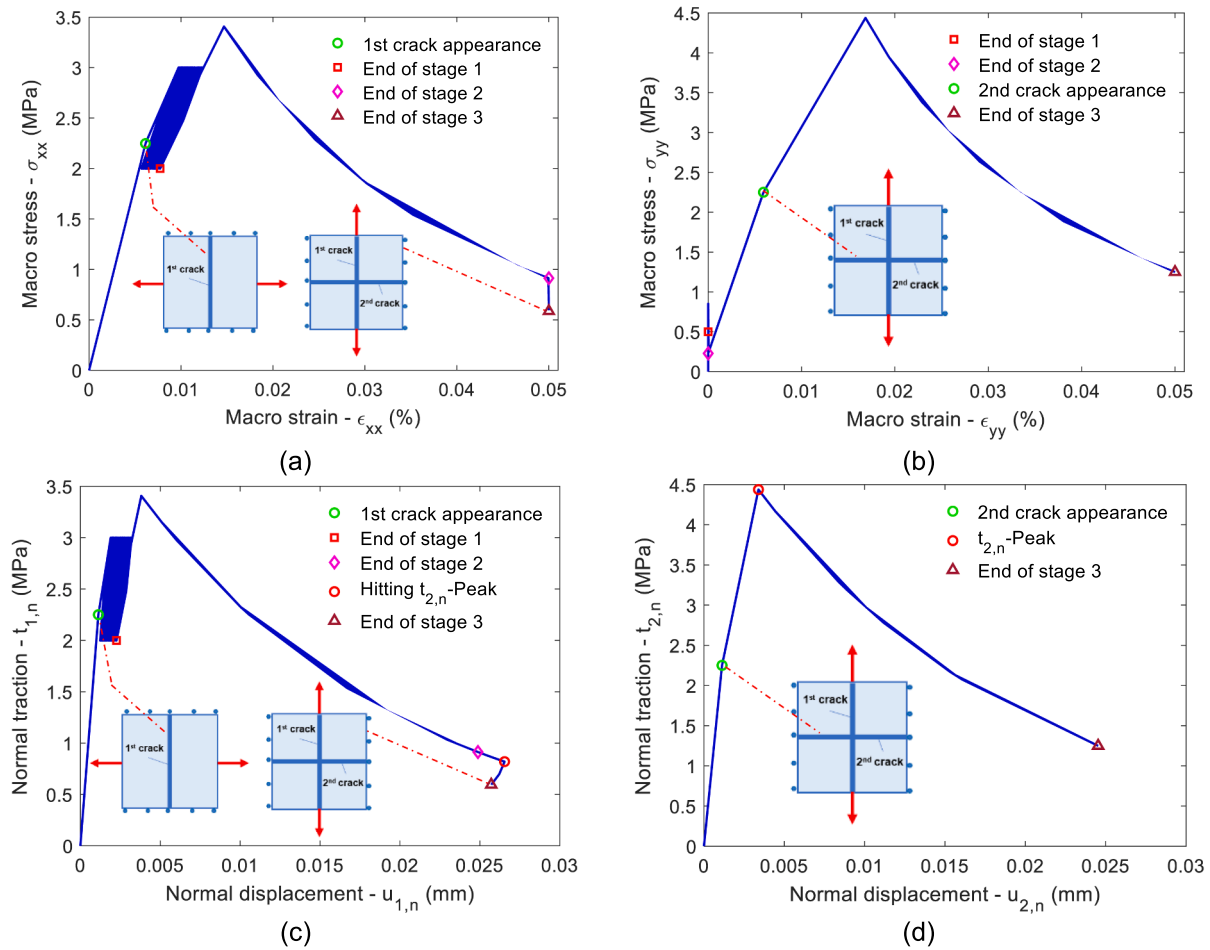
Fig. 14. The behaviour of the two-crack model: (a) Stress–strain curve in the x-direction; (b) Stress–strain curve in the y-direction; (c) Displacement-traction curve of the first crack; (d) Displacement-traction curve of the second crack.

connection. Similar to the macro stress in the x-direction, as the first crack appears, the normal traction of crack 1 ($t_{1,n}$) is 2.25 MPa due to the constraint of traction continuity. Subsequently, the normal-displacement response of crack 1 experiences an elastoplastic behaviour during cyclic loadings in stage 1. This response is followed by hardening and then softening behaviour to reach the value of $t_{1,n} = 0.91$ MPa at the end of phase 2. Meanwhile, the second crack occurs in stage 3 with the value of 2nd normal traction ($t_{2,n}$) being 2.25 MPa which is equal to the value of σ_{yy}. The value of $t_{2,n}$ then undergoes a hardening process to reach the peak of 4.44 MPa before experiencing a softening behaviour. With the presence of two cracks, the element test is now divided into 4 blocks shown in Fig. 14b and d. During the hardening phase to hit the peak, the increase of $t_{2,n}$ and the strain restraint in the x-direction at the third stage make the intact blocks shrink horizontally, causing the first crack to continue opening. This is demonstrated by the rise of normal displacement of crack 1 ($u_{1,n}$) from the end of stage 2 to "Hitting $t_{2,n}$-Peak" in Fig. 14c. However, as $t_{2,n}$ undergoes softening until the end of stage 3, all four blocks expand horizontally, resulting in the closure of the first crack, shown by the decrease of $u_{1,n}$ in Fig. 14c. It should be noted that the softening of $t_{1,n}$ from the end of stage 2 to "Hitting $t_{2,n}$-Peak" in Fig. 14c is due to the opening crack leading to elasto-plastic softening, while stage from "Hitting $t_{2,n}$-Peak" to the end of stage 3 is unloading softening owing to 2nd crack closure.

4.2.4. Model behaviour under complicated loading path (tension, compression and shear) (Example 3)

Sections 4.2.1 and 4.2.3 demonstrate the proposed model's ability to capture cyclic behaviour in the tension domain. However, in reality,

materials can be subjected to complicated loading conditions, which are a combination of tension, compression and shear stresses. Therefore, this section will illustrate the capability of the proposed model under such complex situations. An element test, shown in Fig. 15, is conducted with the same material properties and model parameters as the test in Section 4.2.1, except for $K_n = K_s = 5 \times 10^{12}$ Pa/m, $\psi_t^{ini} = 0.8$, and $\delta_f = 0.5 \times 10^{-3}$ m. The RVE is subjected to three different loading paths where constant shear stress, $\sigma_{xy} = 0.2$ MPa, is applied throughout the test. In the second stage, a cyclic stress amplitude ranging from -1.5 MPa to 2.5 MPa in the x-direction is applied until the number of cycles is 57, followed by a strain-controlled loading up to $\varepsilon_{xx} = 0.02$ %.

The macro and meso behaviours of RVE are plotted in Fig. 16. Unlike Examples 1 and 2, where the crack orientation is perpendicular to the loading direction, the combination of tension and shear stress results in an inclined crack angle of $16°$. This inclined orientation leads to a difference in the lowest and highest stress amplitude between macro and meso behaviour. Specifically, σ_{xx} ranges from -1.5 MPa to 2.5 MPa, while the local normal traction t_n varies from -1.31 MPa to 2.48 MPa. In addition, the slopes of the stress–strain curve and local displacement-traction one reduce under cyclic loading, and this reduction is much more significant for several last cycles. The stiffness distinction is evident when the stress point moves from the tension to the compression domain. This characteristic is owing to the introduction of the Heaviside step function in Eq. (17), which represents the partial recovery of material stiffness in compression because of crack closing. Furthermore, the stiffness distinction in tension and compression regimes is further enhanced by the difference in the failure mechanism of the proposed model, presented in 2.2. The tensile domain failure is governed by
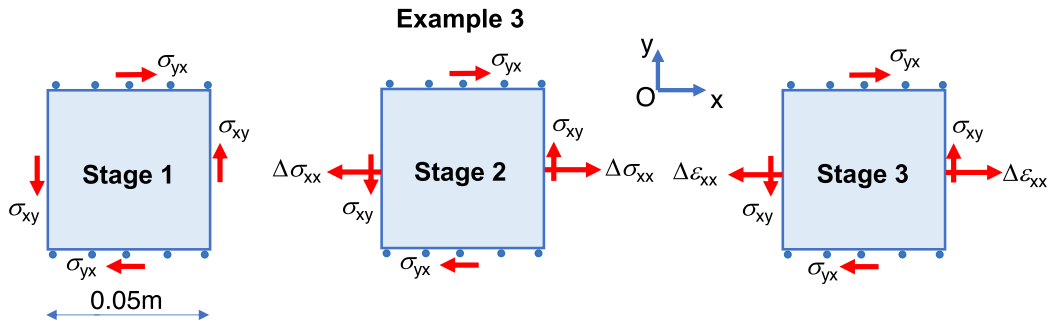
Example 3

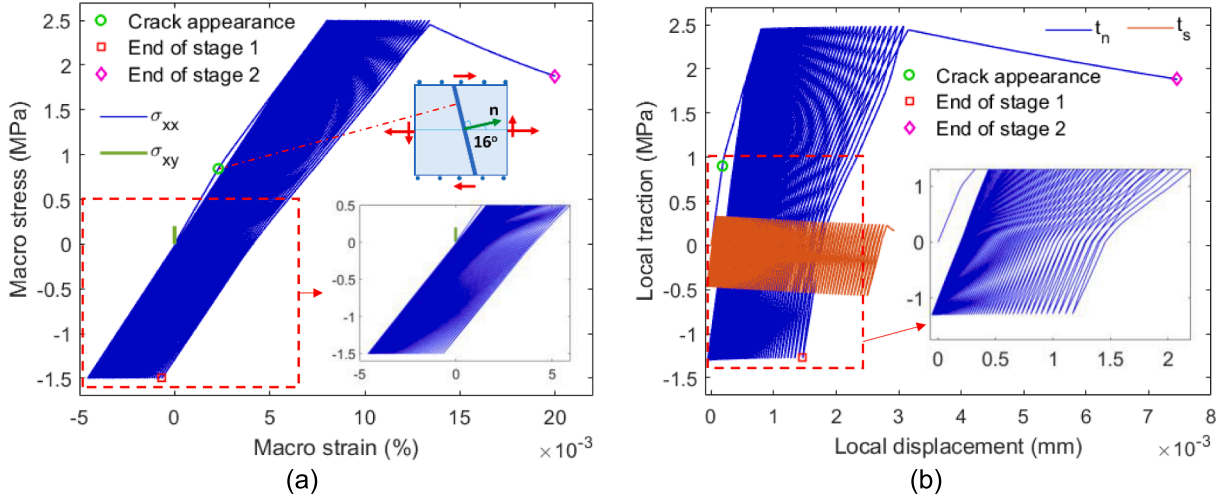**Fig. 15.** Tension, compression and shear loading stages.

Fig. 16. The behaviour of the proposed model under tensile-compressive cyclic loading and shear stress: (a) Macro behaviour of the test; (c) Meso behaviour on the fracture plane.

tensile and shear stress, while shear stress mainly decides the failure in the compression region via the image rule in Eq. (27).

4.3. Model validation against uniaxial cyclic loading

This section highlights the performance of the proposed model in capturing the monotonic and low cyclic response of the material. The model is evaluated against uniaxial tension tests conducted by Gopa-

laratnam and Shah [19]. The properties used in the test are Young's modulus $E = 30$ GPa, Poisson's ratio $\nu = 0.18$, initial cohesion $C^0 = 20$ MPa, tensile strength $f_t^0 = 3.6$ MPa, and $\mu = 0.84$. The elastoplastic parameters of the model are: $\alpha = 0.7$, elastic stiffness $K_n = K_s = 2\times10^{12}$ Pa/m, and L = 83 mm, with fatigue parameters of $\psi_t^{ini} = 0$, $e_{do}^0 = 0.7$, $\delta_f = 0.05\times10^{-3}$ m, $m_1 = 1$, $m_2 = 1$, $Q = 0$ and $\kappa = 1$.

Fig. 17a presents a comparison between the stress–strain response predicted by the proposed model and the experimental data in the
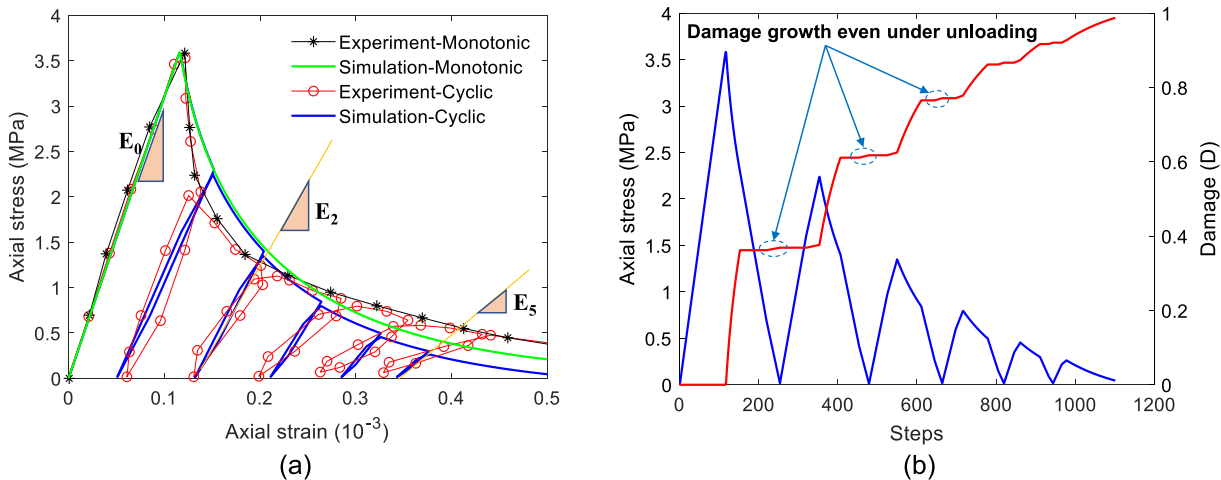
Fig. 17. (a) Macro behaviour of monotonic and cyclic uniaxial tension tests; (b) Axial stress and damage evolution against the number of simulation steps in the cyclic test.

monotonic test. The specific fracture energy produced by the model, represented by the area of the stress–strain curve, aligns reasonably with the one observed in the experiment. In the case of cyclic tests, Fig. 17a illustrates a fair agreement between the proposed model's result and the counterpart. The model can capture sharp softening behaviour in tension, and hysteretic behaviour, as indicated by the difference in the unloading and reloading curves. The areas within hysteresis loops mean that the energy gradually dissipates during a cycle. Due to this dissipation process, the predicted stress–strain curve of the cyclic test lies below the predicted monotonic curve.

In addition, the model can effectively capture residual deformations and the continuous degradation of the material. This degradation is reflected by the decrease in the slopes of the unloading and reloading paths compared to the original stiffness (E_0). The significant stiffness reduction is due to a considerable increase in the damage variable upon cyclic loading even under unloading conditions (Fig. 17b). Although the model effectively captures the cyclic behaviour during the first two cycles, it tends to underestimate the energy dissipation in subsequent cycles. This limitation can be addressed by using the method of controlling dissipation proposed by Nguyen and Korsunsky [45] and Nguyen, Einav and Guiamatsia [43].

5. Finite element analysis (FEA) at structural levels

To demonstrate the performance of the proposed model in capturing the fatigue behaviour of cemented materials, two types of tests are simulated: three-point bending beam and four-point bending specimen tests. The proposed model is implemented into the commercial package ABAQUS for structural analysis, using the user-defined explicit material subroutine VUMAT. Both types of tests in this section consist of two parts: strength/monotonic tests and fatigue tests. The purpose of using strength tests is to determine the peak load which the specimen can carry. The maximum cyclic applied load in the fatigue test is then estimated based on that peak load. The mechanical parameters of material and model parameters needed for fatigue cohesive-frictional models are summarised in Table 1. It is worth noting that the property parameters and elastoplastic parameters are calibrated first against monotonic tests. Based on those, the fatigue parameters are then calibrated from fatigue experiments.

This study uses three-node triangular elements and performs all structural simulations in 2D plane stress. The characteristic length L of

each element is related to the size of the finite element by using the definition $L = \Omega/A$ in Fig. 1. For 2D problems, this length becomes $L = A/l$, wherein A is the area of element and l is the length of fracture plane crossing the element. However, to facilitate the implementation, the characteristic length can be approximated as $L = \sqrt{A}$ [10,31,32,48].

5.1. Three-point bending tests under monotonic and constant amplitude cyclic loadings

In this section, three-point bending tests carried out by Keerthana and Kishen [26] are simulated under strength tests and fatigue tests with constant fatigue loadings to illustrate the capability of the proposed model.

5.1.1. Simulation setup

The strength test of three-point bending beams with structural geometry and boundary condition is shown in Fig. 18a. To reduce the computational cost, half of the beam is simulated in this example with two different meshes, mesh 1 (2251 elements) and mesh 2 (3984 elements), as shown in Fig. 18b and c. For the strength test, the specimen is conducted under a displacement-controlled program with the displacement applied at the middle top of the specimen. However, the fatigue test is carried out under stress-controlled loading with the maximum applied cyclic load of 80% peak load determined in the monotonic test and the minimum value of 0.25 kN.

5.1.2. Model predictions

5.1.2.1. Strength test. The predicted load-crack mouth opening displacement (CMOD) responses are presented in Fig. 19a. The model prediction reasonably agrees with the experiment, exhibiting sharp softening behaviour after the peak due to the brittle nature of concrete behaviour. Furthermore, Fig. 19a indicates the convergence of numerical results with mesh refinement, attributed to the characteristic length L introduced in the double-scale model. Notably, the simulation outcomes in Fig. 19a use the analytical solution to detect crack orientation as presented in Section 3.1. To demonstrate the computational efficiency of this method, the scanning technique with an increment of orientation angle θ equal to 0.1 for every step of crack detection is used for comparison. Both ABAQUS jobs using these methods adopted mesh 2 and were executed using 6 processors based on an Intel Core i7-4790 CPU @3.60 GHz with 16 GB RAM. Fig. 19b shows that the two approaches produce the same results. However, the simulation time with an analytical solution for crack detection was 1.1 min, roughly eleven times shorter than the one with the scanning technique. This comparison illustrates the excellent computation efficiency of the analytical solution for crack detection, and therefore, this method is adopted in the following simulations.

In Fig. 20a, the FPZ shows crack initiation and development at different monotonic test stages. As depicted, the cracks initiate at the notch tip and then propagate upward in stages A and B. Only half of the damaged elements possess two cracks in both phases, and most of the crack orientations are vertical and parallel to the notch. The vertical direction of the crack is due to mode-I failure in the three-point bending test, where the horizontal tensile stresses develop at the notch tip first. In stage C, the cracks continue to spread upward to the top of the specimen, and the majority of damaged elements have two cracks. Although the FPZ develops in a considerable area, the maximum damage variable contours in Fig. 20b demonstrate that only one localised major macro crack formed and propagated during the simulation.

5.1.2.2. Fatigue test under constant amplitude cyclic loading. Fig. 21a illustrates the applied load-CMOD response of the fatigue test under constant loading amplitude. Under fatigue loading, the permanent displacement progressively increases, as shown by the movement of

Table 1
Mechanical properties of material and model parameters.

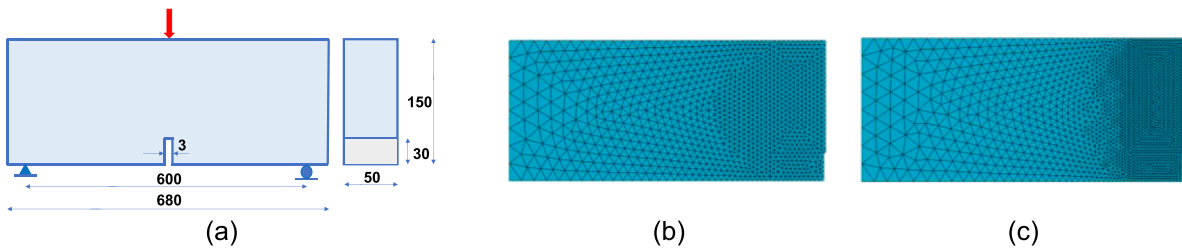| Properties	Example 1 (Section 5.1)	Example 2 (Section 5.2)	Example 3 (Section 5.3)
E(GPa)	18	32	19
ν	0.12	0.2	0.2
C^0(MPa)	25	10	10
f_t^0(MPa)	3.6	4.2	0.6
Elasto-plastic parameters			
$K_n=K_s$ (Pa/m)	2.0×10^{13}	1.6×10^{13}	5.2×10^{13}
μ	0.754	0.754	0.364
α	1.1	1.7	1.4
β	0.1	0.1	0.01
Fatigue parameters			
ψ_t^{ini}	0.52	0.15	0.52
e_{do}^0	0.05	0.65	0.1
Q	9	0	13
κ	1.5	2	5
δ_f(m)	4.3×10^{-6}	1.65×10^{-7}	3×10^{-7}
m_1	11	10	20
m_2	15	4	4
G_c(N/m)	119	–	28
C_{jump}	0.002	–	0.14
m_{jump}	1.0	–	1.0

Fig. 18. Specimen geometry and mesh sizes for the three-point bending test: (a). Geometry; (b) Mesh 1; (c) Mesh 2.
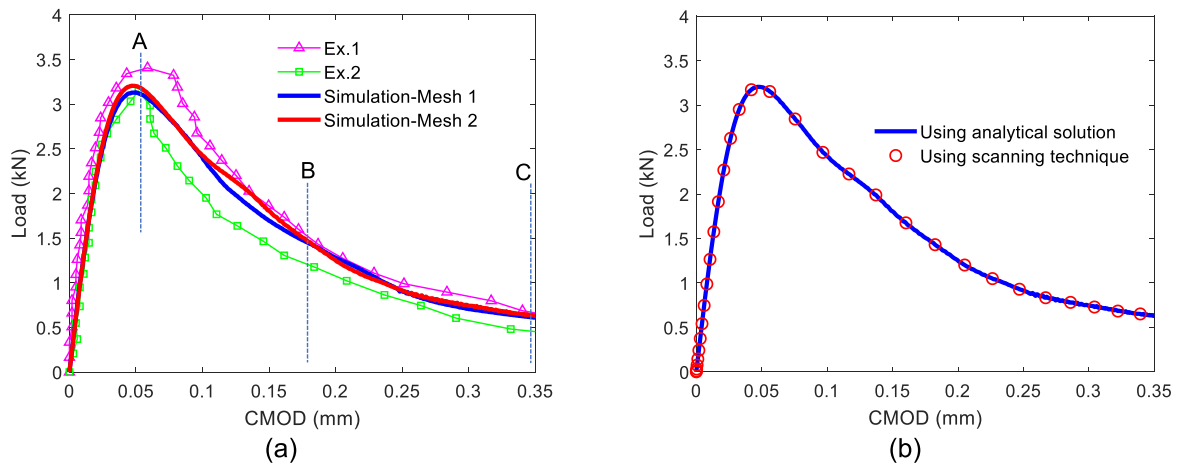

Fig. 19. Load-CMOD responses for strength test of three-point bending beam: (a) Comparison of experiment and simulation; (b) Comparison between simulation result using the analytical solution to detect crack and the one using scanning technique for crack detection.
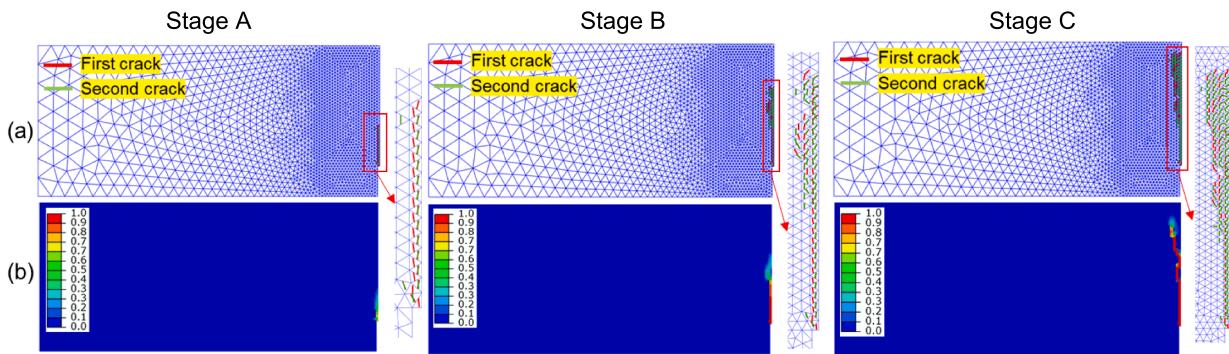

Fig. 20. (a) The FPZ around the crack tips at different stages (shown in Fig. 19a) of the strength test (mesh 2); (b) The maximum damage contours between two damage variables of two cracks at different stages.

CMOD at the end of the unloading path away from the origin. Since there is a lack of experimental data on the CMOD-number of cycle curves, a comparison using CMOD-normalised cycle curves between the experimental and simulation results is presented in Fig. 21b. As illustrated, the proposed model demonstrates its ability to capture fatigue response with a fair agreement between the simulation result and experimental data. CMOD grows dramatically at first, followed by a stable stage and a rapid increase toward the end. The macro behaviour of the specimen, represented by CMOD evolution, results from the collective response of behaviours on fracture planes and surrounding bulks. Thanks to the competitive fatigue mechanism of the fatigue rule in Eq. (28) to describe the behaviour of fracture planes, the proposed model can fairly capture the three distinct phases of CMOD development.

One of the key features of the proposed model, compared to most of the models in the literature review, is its capability to simultaneously describe the distinct behaviours of the meso scale (i.e. fracture planes

and macro scale. Fig. 22 illustrates the evolution of horizontal stress, normal traction, and damage variables at different loading cycles. As can be seen, the residual horizontal tensile stress zone and residual normal traction zone initiate around the crack tip, which is the weakest area of the beam. Under further cyclic loadings, these zones move upward, and there are reductions in the values of σ_{xx} and $t_{1,n}$ vertically far away from the notch tip shown in Fig. 23a and b. For the first cycle, the maximum values of σ_{xx} and $t_{1,n}$ are smaller than tensile strength of material (i.e. f_t^0 = 3.6x10^6 Pa). Then, these values experience significant drops, and their peaks keep translating away from the tip. The drops in values of σ_{xx} and $t_{1,n}$ illustrate that softening behaviour has occured in the beam. Similarly, the damage variable zone occurs at the notch tip for the first cycle. This zone then expands in size and moves upward until the beam fails (Fig. 22c). The value of the maximum damage variable is also plotted in Fig. 23c to indicate the evolution of the damage zone during cyclic loadings. The damage variable starts with a substantial value of roughly
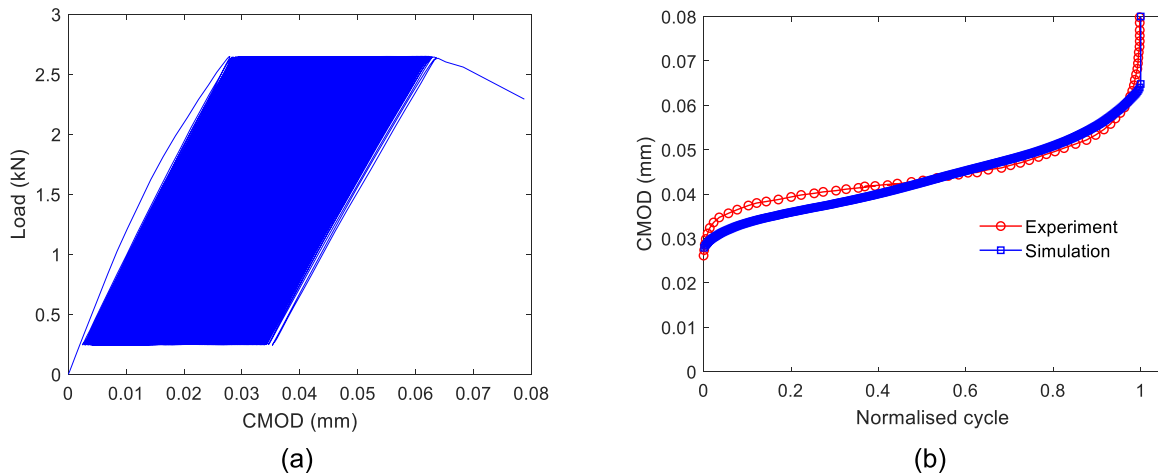
Fig. 21. (a) Load-CMOD response of fatigue test under constant loading; (b) Comparison between fatigue simulation and experimental data.
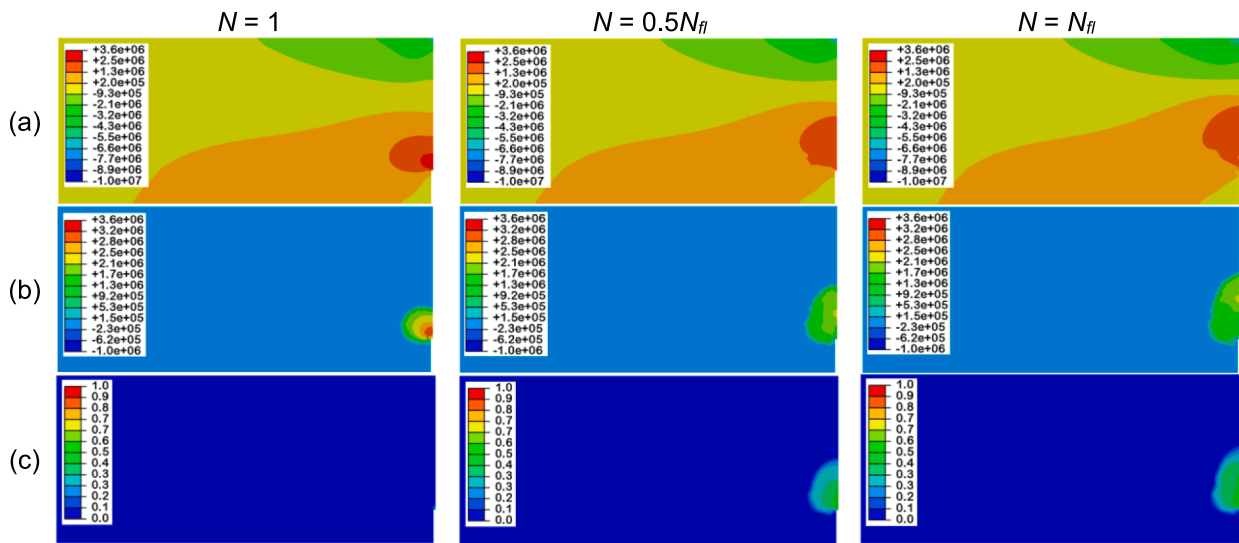

Fig. 22. Details of three-point bending beam fatigue test at the different number of cycles: (a) Horizontal stress (Pa) (mesh 2); (b) Normal traction of primary crack; (c) The maximum total damage variable contours between two damage variables of two cracks.
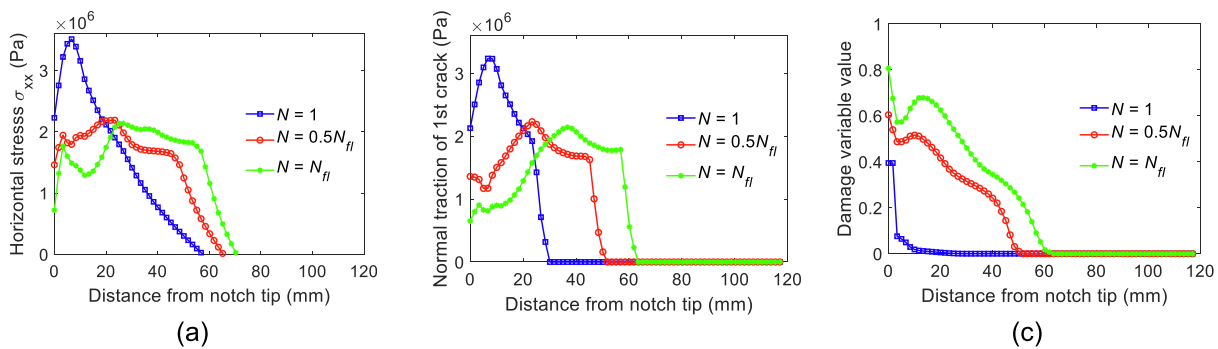

Fig. 23. Details of three-point bending beam fatigue test corresponding to the centre line of the beam: (a) Softening behaviour of horizontal stress; (b) Softening behaviour of normal traction of primary crack; (c) Maximum damage evolution.

0.4, then experiences a stable increase for the cycle $N = 0.5N_{fl}$ (N_{fl} is the number of cycles to reach failure), followed by a maximum value of nearly 0.81 when the beam ruptures.

This research investigates the FPZ, crack orientations, and their evolutions during the fatigue test, as shown in Fig. 24. The FPZ initiates

at the notch tip and has a circle shape for the first cycle. Most of the crack orientations near the tip and the centerline of the beam are nearly vertical, while those far from the tip tend to be inclined. As the number of loadings increases, the size of FPZ grows and moves upward, with most of the damaged elements featuring two cracks. The enlargement of FPZ
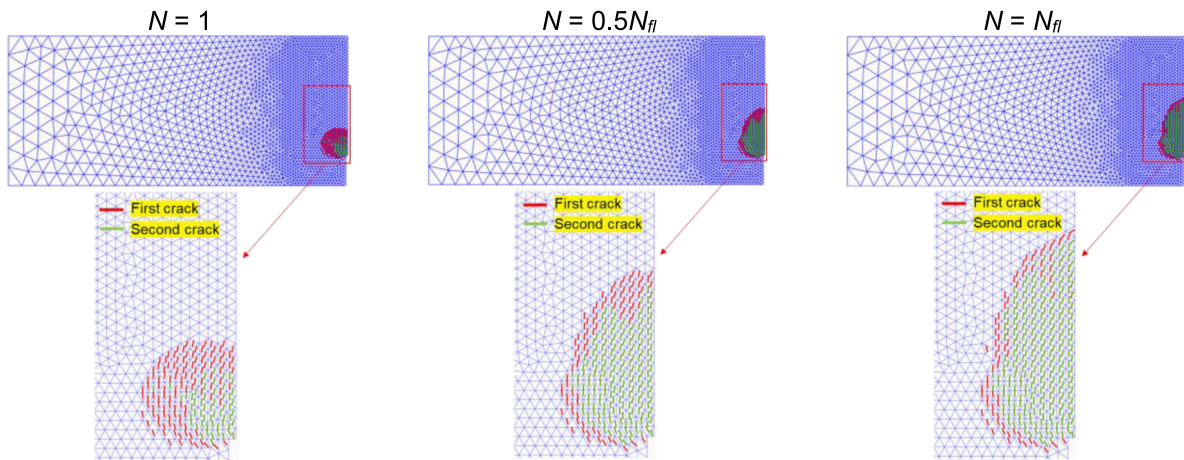
Fig. 24. The FPZ around the crack tips at different stages of the fatigue test (mesh 2).

is caused by the loss of material strength around the notch tip first, as shown in Fig. 23a and b. With the increasing number of cycles, this loss helps stresses transfer upward, resulting in new cracks initiating and propagating. At the last cycle, the fatigue test fails suddenly with a great curved shape of FPZ around the notch tip and the centre line of the specimen. This rupture differs from the FPZ in the monotonic test, where the failure of the strength test is gradual, with a maximum damage value of 1.0, and the FPZ looks like a narrow zone (Fig. 19b). This distinction could be due to two reasons. The first is the difference in the applied load between the two tests, with the monotonic test using a strain-control program and the fatigue test using a stress-control program. The second primary reason is the failure mechanism between them. While the monotonic test undergoes continuous loading, the fatigue test experiences a loading and reloading process. The cyclic process causes the accumulated stress intensity factors to increase (K_I) at the area around the notch. As K_I reaches a critical value, stability is lost, and the specimen ruptures dynamically [27,28].

5.2. Three-point bending tests under monotonic and cyclic loading with variable amplitudes

In Section 5.1.2.2, the proposed model shows its capability to capture the fatigue behaviour under constant cyclic loading. Nevertheless, the structures in reality can be subjected to variable loading amplitudes. This variation in loading can involve sudden overloads, leading to crack growth acceleration. Therefore, this section will illustrate the ability of the proposed model to capture the effect of such excesses. To this end, the experiment conducted by Baktheer et al. [5] is simulated.

5.2.1. Simulation setup
The structural geometry and boundary condition of the three-point bending specimen are shown in Fig. 25a. Half of the beam is simulated with two different meshes, mesh 1 (1370 elements) and mesh 2 (2562 elements), as shown in Fig. 25b and c, respectively. The

displacement-controlled program is used for the strength test, with the applied displacement at the middle top of the specimen. In contrast, the fatigue test is conducted under cyclic variable loading with a 40 Hz frequency waveform. During the fatigue test, the lower load level is kept constant at $S_{min} = 0.1Peak$, wherein *Peak* is the peaking loading determined in the monotonic test. However, the upper load varies during the test, starting at $S_{max} = 0.5Peak$ and gradually rising every 10 cycles by $\Delta S = 0.05$.

5.2.2. Model prediction

5.2.2.1. Strength test.
The applied load against the crack tip opening displacement (CTOD) curve in Fig. 26a illustrates a satisfactory agreement between predicted and experimental responses. Due to the displacement-control program used in the monotonic test, the load-CTOD curve experiences a rapid softening behaviour after hitting the peak load, followed by a gradual decrease at the final stage of failure. Besides, Fig. 26a also indicates similar numerical outcomes with two different meshes, demonstrating the numerical convergence upon mesh refinement again. The evolution of FPZ and crack pattern obtained from the proposed model, represented by damage contour, are illustrated in Fig. 26b and c. Throughout the simulation, only one localised significant macro fracture emerges at the notch tip and then propagates upward with the maximum value of the damage variable of 1.

5.2.2.2. Fatigue test under variable loading.
Fig. 27a shows the applied load-CTOD response of the fatigue test under variable loading amplitude. The translation of CTOD at the end of the unloading path, away from the origin, indicates the progressive growth of the permanent displacement. The proposed model is capable of capturing explicit hysteresis loops, which become more pronounced with increasing load levels. The distance between consecutive loops represents a progressively dissipated energy, but this energy dissipation is non-linear during
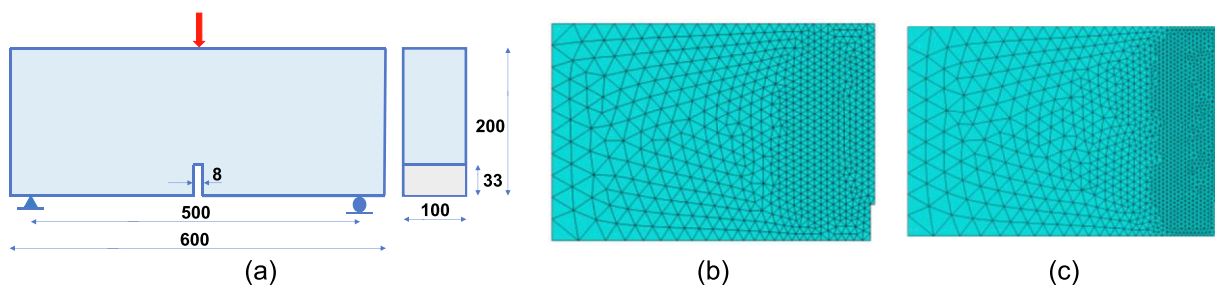

Fig. 25. Specimen geometry and mesh sizes for the three-point bending test: (a). Geometry; (b) Mesh 1; (c) Mesh 2.

(a)

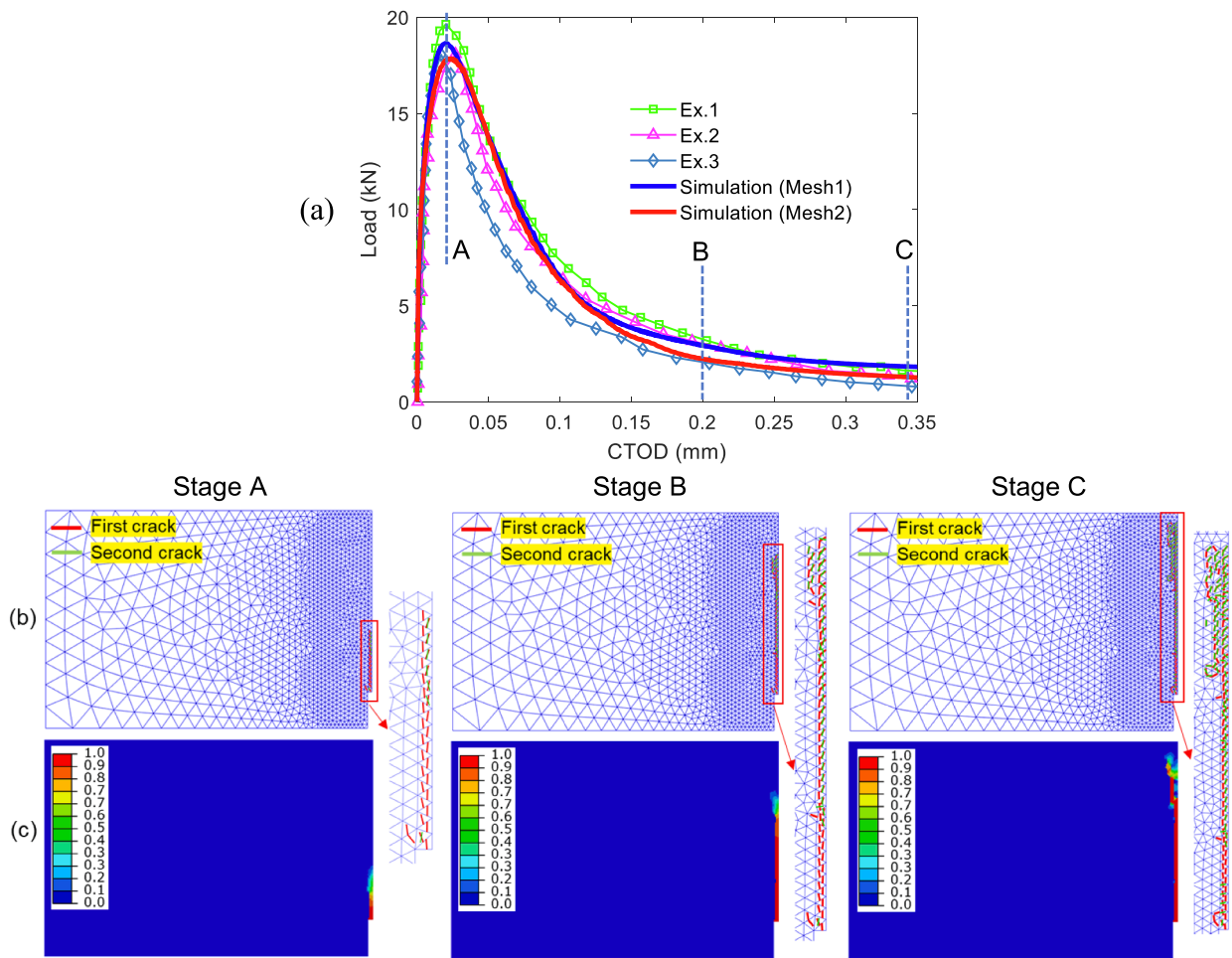**Stage A**   **Stage B**   **Stage C**

Fig. 26. (a) Load-CTOD responses for strength test of three-point bending beam; (b) The FPZ around the crack tips at different stages of the strength test (mesh 2); (c) The maximum damage contours between two damage variables of two cracks at various stages.
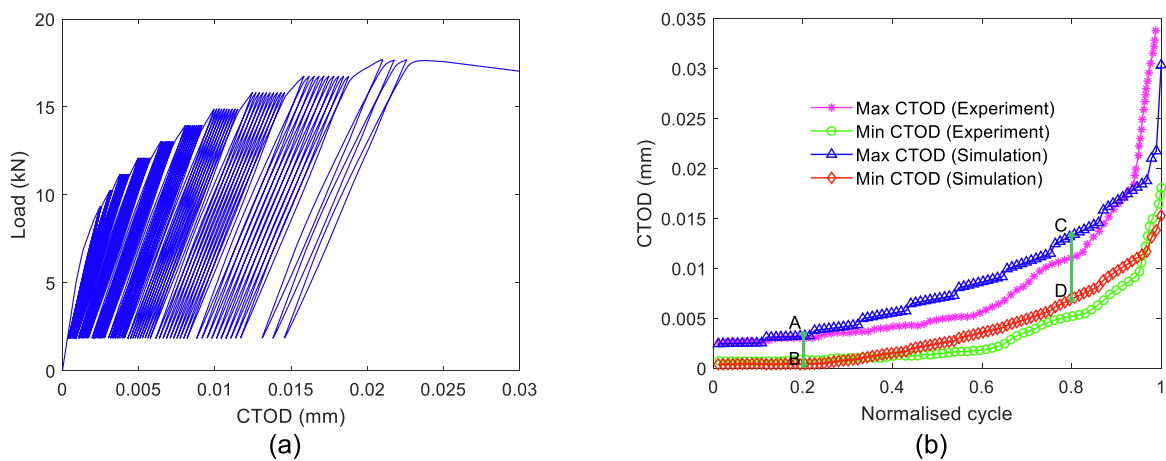

(a)   (b)

Fig. 27. (a) Load-CTOD response in the fatigue test under variable loading; (b) Comparison between maximum and minimum CTOD of simulation results and that of experimental outcomes.

fatigue loading. This nonlinearity is observed in Fig. 27b, where the maximum and minimum CTOD experience a slight increase initially, followed by a significant rise and finally, a sharp increase towards the end of the test. In addition, the proposed model fairly reproduces the trend of a greater distance between the maximum and minimum CTOD under a rising number of cycles compared to experimental data. This trend is illustrated by a shorter distance of line AB at a small normalised

cycle of 0.2 and a longer distance of line CD at a large normalised cycle of 0.8 in Fig. 27b. The greater distance indicates an increasing permanent displacement that occurred within the specimen. In other words, the sample undergoes a degradation of the elastic energy during cyclic loading. Thus, the necessity to assume the loss of the elastic domain of the subloading surface upon damage evolution in Eq. (25) is demonstrated.
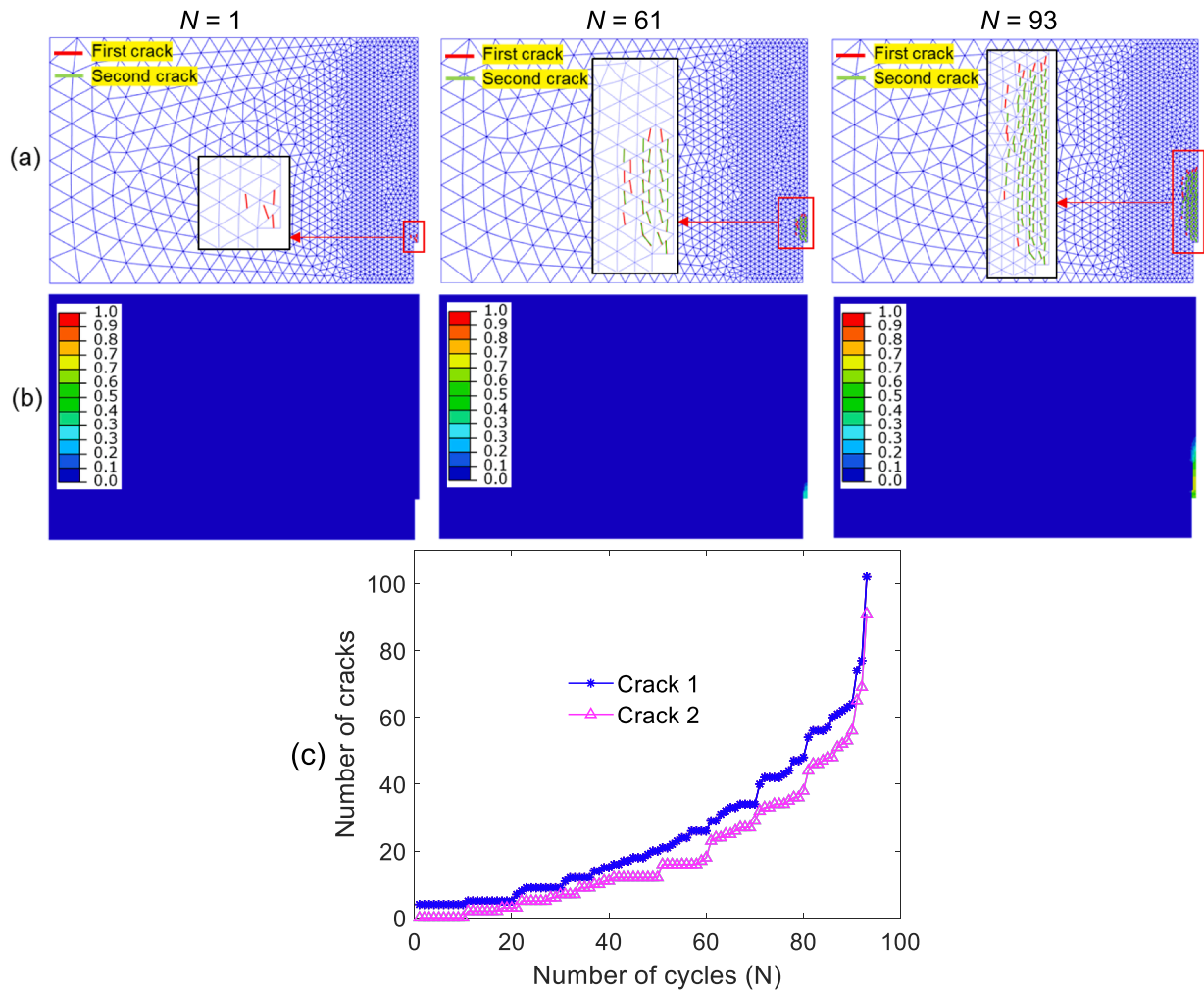
Fig. 28. (a) The FPZ around the crack tips at different stages of the fatigue test (mesh 2); (b) The maximum damage variable contours between two damage variables of two cracks; (c) The evolution of the number of cracks during the fatigue test.

To show the effect of overloads on the beam behaviour, the FPZ, damage contours, and the development of crack numbers are illustrated in Fig. 28. The FPZ initiates around the notch tip with only four cracks developing during the first cycle, while the second crack emerges in cycle 11. However, under further loadings, the number of both cracks increases significantly, especially when sudden loads are applied (e.g.

cycles 70, 80 and 90). At the end of the fatigue test, the FPZ has a curved shape around the notch and the centreline of the beam, which contrasts with the thin FPZ in the strength test depicted in Fig. 26b. Furthermore, most degraded elements experience 2-crack developments at cycles 92 and 93 (Fig. 28a and c).

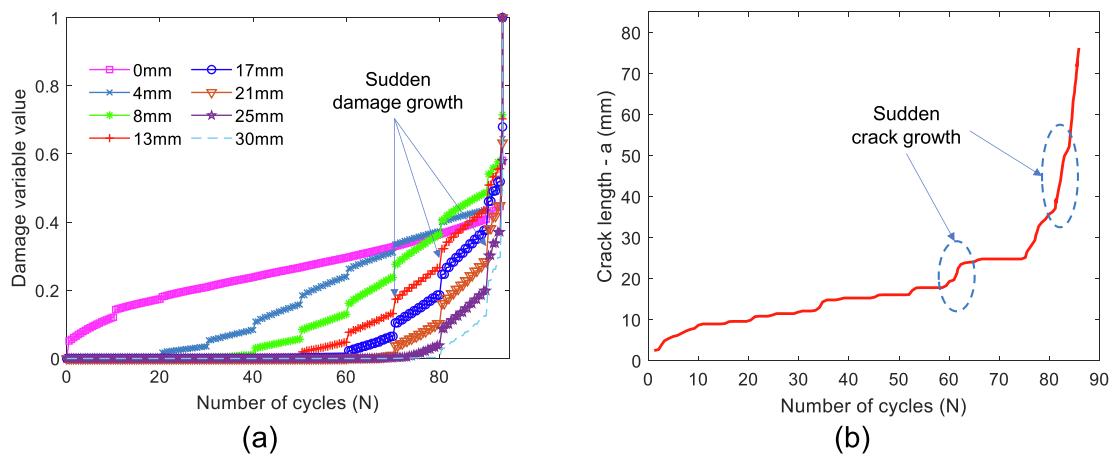For a more qualitative investigation of the influence of overloads, the

Fig. 29. (a) The evolution of maximum total damage variable vertically away from the notch tip; (b) The development of crack length obtained from the experiment (after Baktheer and Becks [6]).

damage variable of degraded elements vertically away from the notch tip is plotted in Fig. 29a. The damage value of the element at the notch tip (i.e. 0 mm) increases significantly for several first cycles. Meanwhile, the damage variables start later as the degraded elements are further away from the notch tip. The non-simultaneous damage development of these degraded elements indicates the propagation of a bottom-up cracking path within the specimen. When the load amplitudes suddenly increase, such as at cycles 70, 80 and 90, the damage values grow rapidly. Therefore, this sharp jump shows a strong influence of sudden loads on the damage development, which is associated with the rapid rise of maximum CTOD in Fig. 27b. The crack length as a function of the number of cycles obtained from the experiment is also plotted in Fig. 29b for comparison with simulation results. As can be seen, the crack length suddenly increases upon rising applied loads. This sudden growth is consistent with the rapid development of damage variables representing the propagation of a crack in continuum damage mechanics. The damage variables rise quickly to reach the maximum value of 0.72 when the beam ruptures at cycle 93, which is close to the fatigue life of 86 cycles obtained from the experimental data.

5.3. Four-point bending tests

In examples 1 and 2, the fatigue responses of notched structures (three-point bending beams) are examined with the FPZ starting at and developing near the notch tip. However, the evolution of the FPZ in unnotched structures is another important consideration. Therefore, four-point bending tests (un-notched specimens) performed by Sounthararajah et al. [61] are examined to observe how the FPZ evolves by simulating them under fatigue tests at a single stress level. The sensitivity of fatigue lives of cemented material to various stress levels is then demonstrated by the proposed model, showcasing its capabilities.

5.3.1. Simulation setup

Fig. 30a illustrates the structural geometry and boundary condition of the four-point bending beam. In this example, half of the beam is simulated with two different meshes, mesh 1 (1532 elements) and mesh 2 (3388 elements), as shown in Fig. 30b and c. The strength test is conducted under a stress-controlled program. During the applied loading process, the applied load, P, and mid-span deflection, δ, are recorded. Based on that, the flexural stress, flexural strain and flexural modulus are calculated as follows [4]:

$$\varepsilon_f = \frac{108H\delta}{23L^2} \tag{51}$$

$$\sigma_f = \frac{PL}{BH^2} \tag{52}$$

$$E_f = \frac{23P_mL^3}{108\delta_mBH^3} \tag{53}$$

where ε_f is the flexural strain, L is the span length, H is the mean beam height, B is the mean beam width, σ_f is the flexural stress, E_f is the flexural modulus, P_m is the maximum magnitude of applied cyclic load and δ_m is the sample deflection corresponding to P_m.

After obtaining the results of the strength test in Section 5.3.2.1, the fatigue test in Section 5.3.2.2 is simulated under a stress-controlled program with a maximum load of 858 N and a minimum load of 50 N. The maximum load corresponds to 77% of the peak load of the strength test.

5.3.2. Model predictions

5.3.2.1. Strength test.
The proposed model shows satisfactory agreement with the experimental stress–strain curves, as seen in Fig. 31a. The curves display hardening behaviour until the sudden rupture of the sample. The convergence of numerical results is also demonstrated by the minor differences between the two different mesh outcomes.

5.3.2.2. Fatigue failure mechanism under one specific stress level.
The proposed model produces a modulus reduction curve that closely matches the experimental results (Fig. 31b). The curve exhibits three distinct phases: a significant drop in the first phase, a gradual decrease in the second phase, and a rapid decline in the final phase. This agreement between the model and experimental data further confirms the model's effectiveness.

To investigate the evolution of macro and meso behaviours under fatigue loading, their corresponding responses at the maximum load of cycles 1, 6011 and 9052 are presented in Fig. 32 and Fig. 33. The residual horizontal tensile stress zone, which represents macro behaviour, initially develops at the bottom and middle of the beam. As the number of cycles increases, the zone expands upward, as indicated by the evolution of σ_{xx} along the section cut A-A (Fig. 32c). During the loading process, the horizontal stress decreases, showing that softening behaviour has occurred in the specimen. Similarly, the damage zone also grows with repeated loadings. For cycle 1, this zone initiates at the middle bottom of the specimen with the maximum damage value of 0.015 along section cut A-A. However, the damage zone at cycle 6011 tends to localise in the middle of the specimen, about 20 mm from the bottom. Interestingly, a small second damage zone appears at cycle 6011, which grows to reach a maximum damage value of about 0.17 for the last cycle (Fig. 32c). Although the damage zone undergoes the localised processing in the middle region, the specimen fails suddenly in the last cycles with a bottom-up damaged domain (Fig. 32b).

Besides the macro response, the meso behaviour on fracture planes in Fig. 33 is also noteworthy. Fig. 33a and b illustrate the normal and shear tractions of the primary crack. For the first cycle, the normal and shear traction zones appear at the bottom middle of the beam, and these zones move upward under further cyclic loadings. During the loading procedure, the normal traction of the first crack experiences a significant reduction until the sample fails (Fig. 33c). The value of $t_{1,n}$ at the bottom of the beam is roughly 5.9×10^5 Pa for the first cycle, which is slightly smaller than the tensile strength of the four-point bending specimen (i.e. 6.0×10^5 Pa). This smaller value is due to the small damage process that occurs in the beam. The normal-traction value continues to decrease until reaching the final cycle. The decline in material strength is due to the development of the damage variable, presented in Fig. 32c. However, the value of shear traction increases along the section cut C–C since it has not reached the shearing strength of the material. It is worth noting that zero values of normal and shear tractions in Fig. 33c mean that no cracks have appeared in this region.
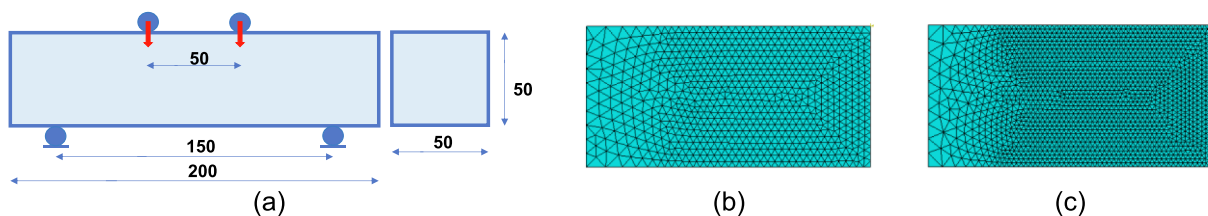

Fig. 30. Specimen geometry and mesh sizes for four-point bending test: a. Geometry; (b) Mesh 1; (c) Mesh 2.
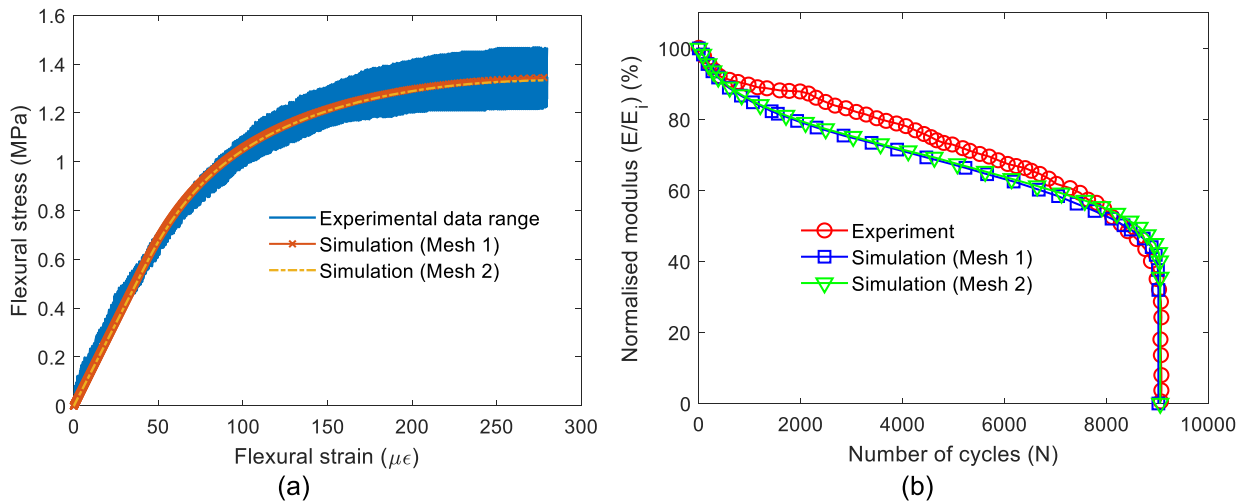
Fig. 31. (a) Stress–strain responses for strength tests of four-point bending beam; (b) Modulus reduction curves in the fatigue tests.
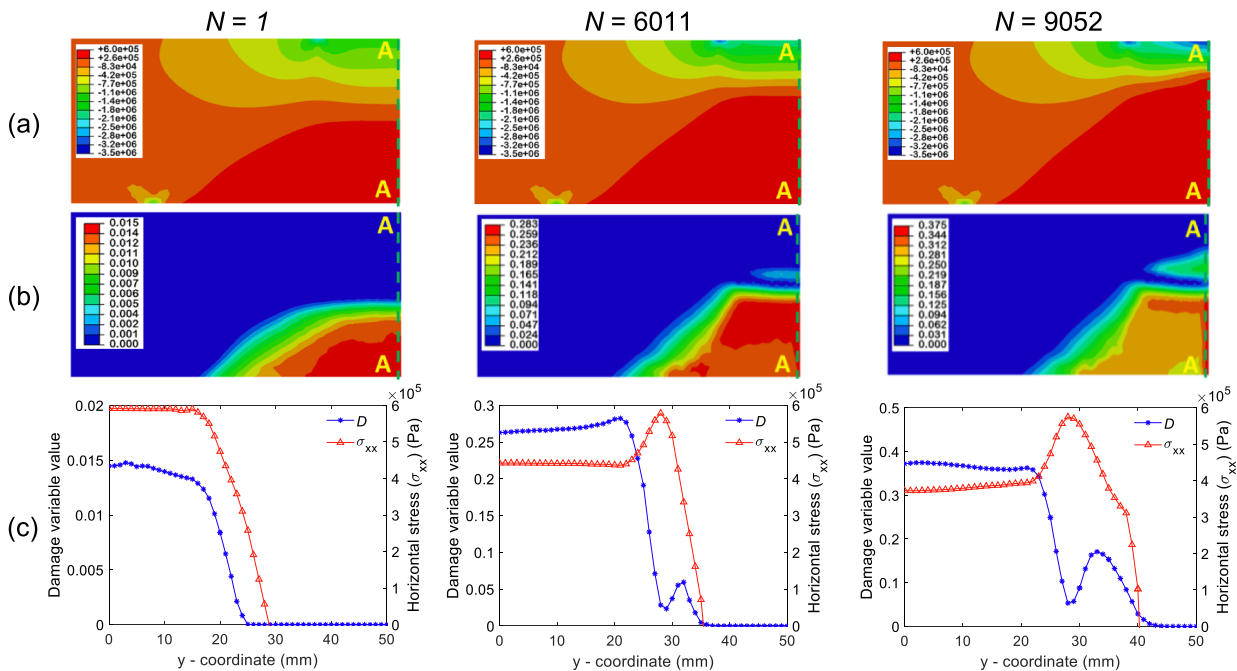

Fig. 32. Details of 4-point bending beam fatigue test at the different number of cycles: (a) Horizontal stress (Pa) (mesh 2); (b) Maximum total damage contour profiles; (c) Corresponding section cut of horizontal stress and maximum damage variable values.

Moving on to the initiation and evolution of FPZ of the un-notched fatigue test, this section describes the development of FPZ at different stages of the fatigue test, as illustrated in Fig. 34a. The contours of crack orientations are also plotted in Fig. 34b and c. For cycle 1, the FPZ emerges in a large area at the bottom and middle of the specimen. Two significant regions with two failure modes exist. The mode-I failure occurs at the centre and bottom of the beam, whereas the region below the loading position experiences mixed-mode failure. Regarding the mode-I failure domain, the crack orientation is nearly 0° or 180°, indicating that normal vectors of cracks are horizontal. These horizontal crack orientations can be explained by the meso-scale model used for crack initiation in section 2.2. At the bottom and middle of the specimen, the horizontal stress is dominant, hence normal tractions develop and contribute to the mode-I cracking. On the other hand, the domain below the loading position is subjected to the bending moment and shear force caused by the external loading. As a result, normal and shear tractions grow (Fig. 33a and b), leading to mix-mode failure. Under additional

cyclic loadings, the FPZ enlarges its size and translates upward, represented by new crack initiations and developments shown in Fig. 34a. The evolution of FPZ is attributed to the loss of material strength in the specimen. At the last cycle, the FPZ mainly develops upward, consistent with the appearance and propagation of the small second damage zone in Fig. 32b.

5.3.2.3. Fatigue failure under different stress levels. The fatigue characteristics of the material are generally represented by the Wöhler or S-N curves. These are semi-logarithmic curves obtained by the construction of a relationship between the maximum applied stress levels and the fatigue life (N_f or N_{fl}). Due to their effectiveness in estimating the fatigue life of materials, the S-N curves are commonly used in practical designs or research. This section aims to demonstrate the capability of the proposed model to capture the sensitivity of stress levels on fatigue lives.

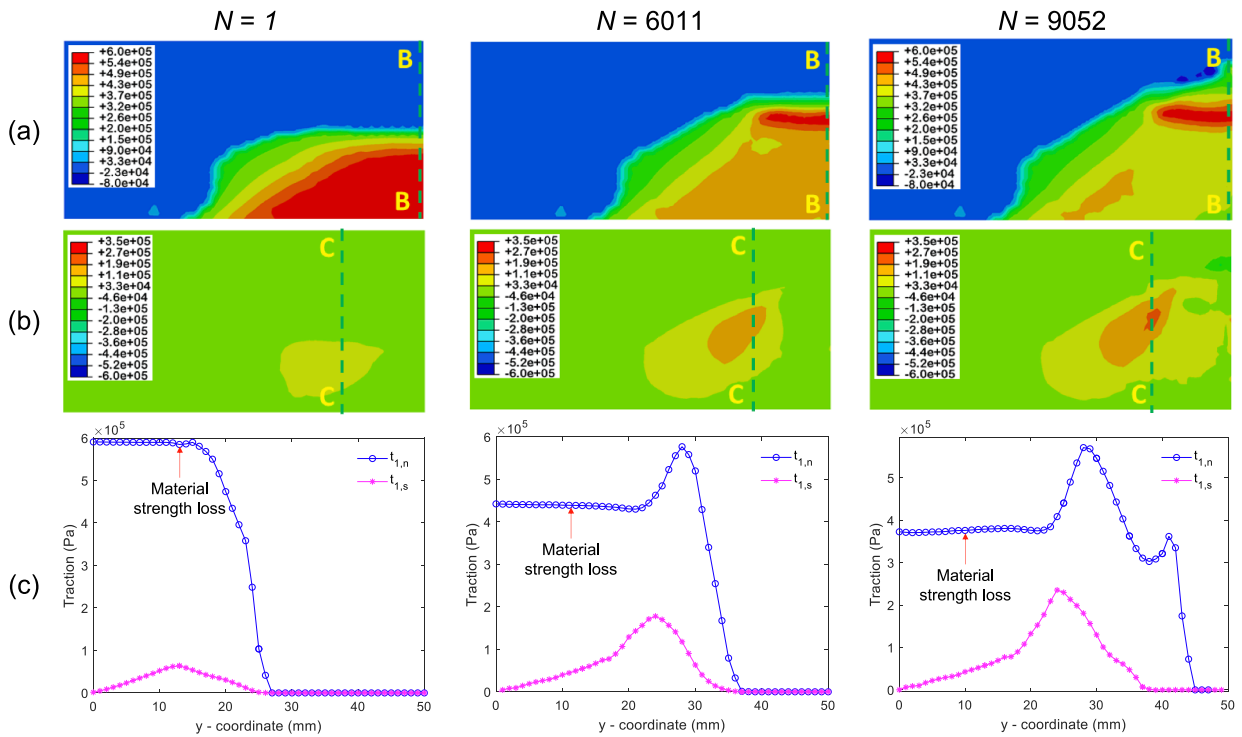The four-point bending fatigue test in section 5.3.2.2 is further

Fig. 33. Details of 4-point bending beam fatigue test at the different number of cycles: (a) Normal traction on primary crack (Pa) (mesh 2); (b) Shear traction on primary crack (Pa); (c) Corresponding section cuts of traction values.
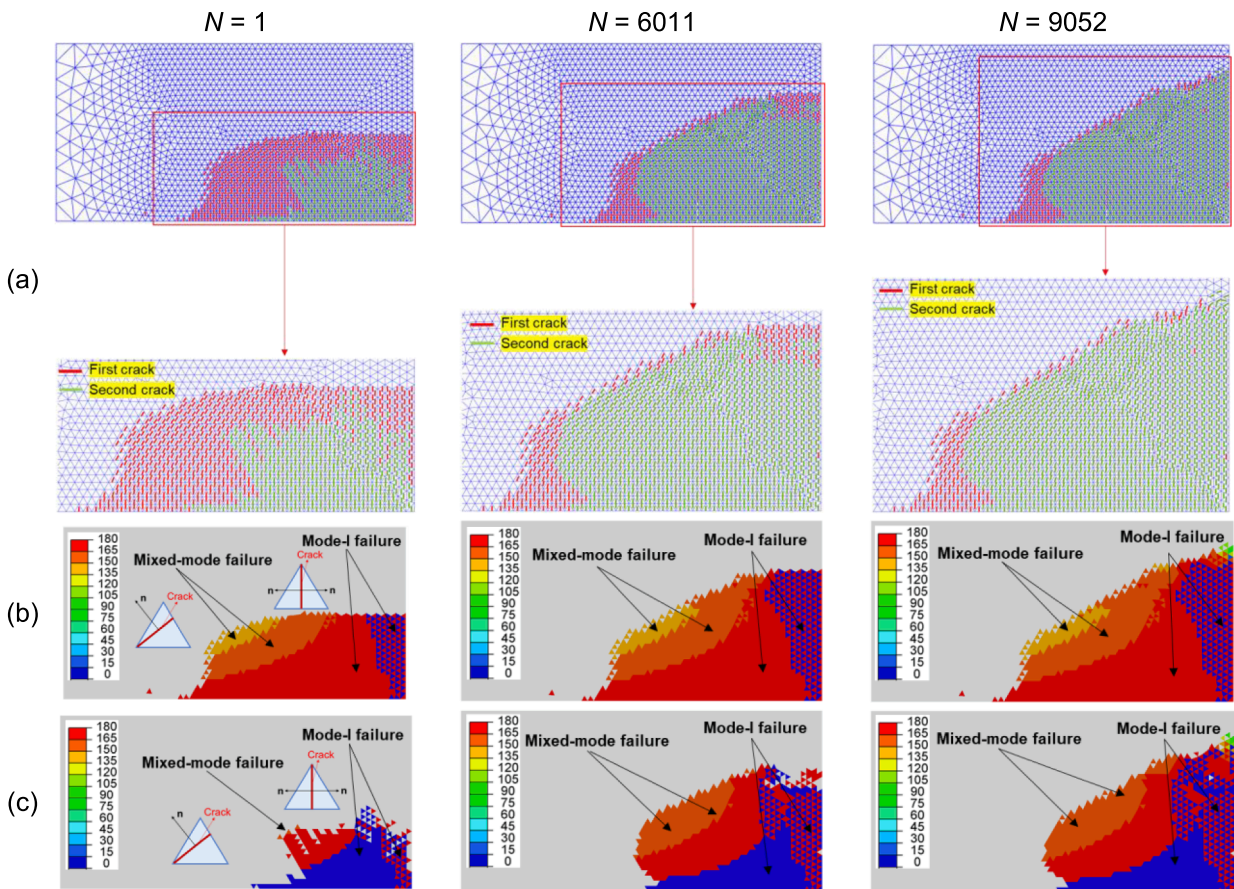

Fig. 34. (a) The FPZ around the crack tips at different stages of the 4-point bending fatigue test; (b) First crack orientation contours (grey domain means no cracking); (c) Second crack orientation contours.
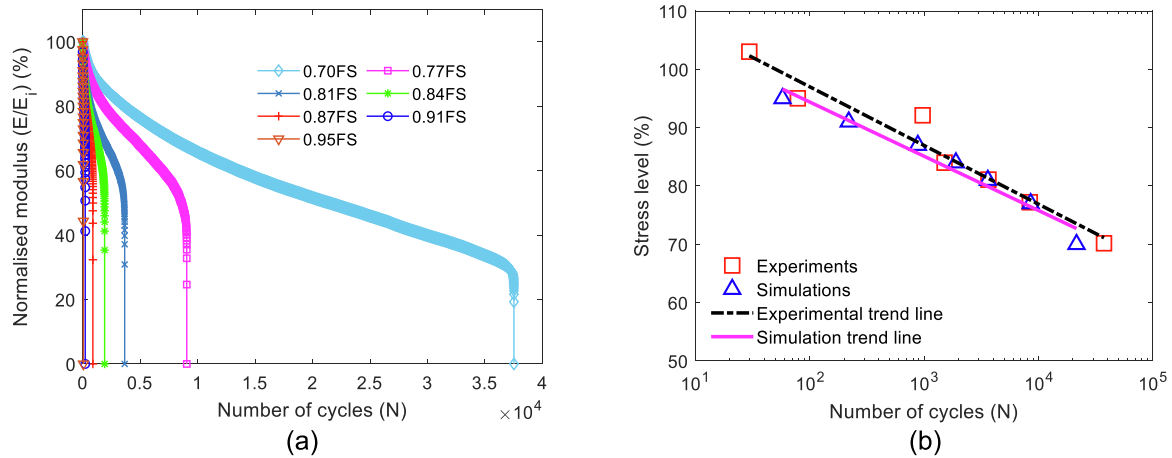
Fig. 35. (a) The numerical outcomes of modulus reduction against the number of cycles under different stress levels; (b) The S-N curves.

analysed by applying different load levels, from 70% to 95% of flexural strength (FS). As shown in Fig. 35a, under increasing stress levels, the rate of modulus reduction experiences a significant increase, leading to earlier beam specimen failure. To provide more insights, the S-N curves are plotted in Fig. 35b, where the fatigue life (N_f) is defined as the cycle to reach a 50% decrease in modulus according to Austroads [4]. The figures demonstrate the strong effects of stress amplitudes on the lives of specimens, where higher stress levels result in smaller fatigue lives. Moreover, the proposed model is shown to effectively capture these influences, as evidenced by the fair agreement between the simulation trend line and the experimental data (Fig. 35b).

To explain the mechanism of how the applied loads affect the fatigue lives, Fig. 36 presents the total damage profiles of specimens at different stress levels and cycles. In the early cycles, higher stress amplitudes cause fracture planes to occur sooner in the specimen, leading to larger damage zones. Although the maximum value of the damage is really small for all stress levels at cycle 1, the accumulated damages develop differently at the time of $N = 0.5N_f$ and $N = N_f$. In the latter case, the maximum damage of the specimen with 0.70FS and 0.81FS is 0.449 and 0.318, respectively, whereas that of the sample under 0.95FS is only 0.262. This significant difference is because, at increased stress levels, the damage tends to be focused on weaker areas, resulting in fracture

failure without sufficient cumulative growth of fatigue damage. Consequently, the beam with a higher stress level fails with a lower total damage variable value. Our cohesive-frictional fatigue model accounts for the sensitivity of load amplitudes at the constitutive level through the interpolation rule in Eq. (27). Therefore, the model can capture the impact of stress levels on fatigue lives by the collective response of behaviours on fracture planes and surrounding bulks.

6. Conclusion

This work addresses the necessity and benefits of accounting for the failure mechanism at the mesoscale in modelling fatigue responses of materials. The fatigue-induced damage occurring on fracture planes serves as a basis for developing a novel size-dependent constitutive fatigue model. This new model features an intrinsic length, which automatically ensures the convergence of numerical results for different spatial discretisations. In addition, the structure of the developed model contains the interactive responses of both the bulk material and two fracture planes, which are governed by a cohesive-frictional fatigue model. This proposed cohesive model couples damage mechanics and bounding surface theory to capture nonlinear fatigue responses (i.e., fatigue damage growth, hysteresis and three stages of fatigue failure) in
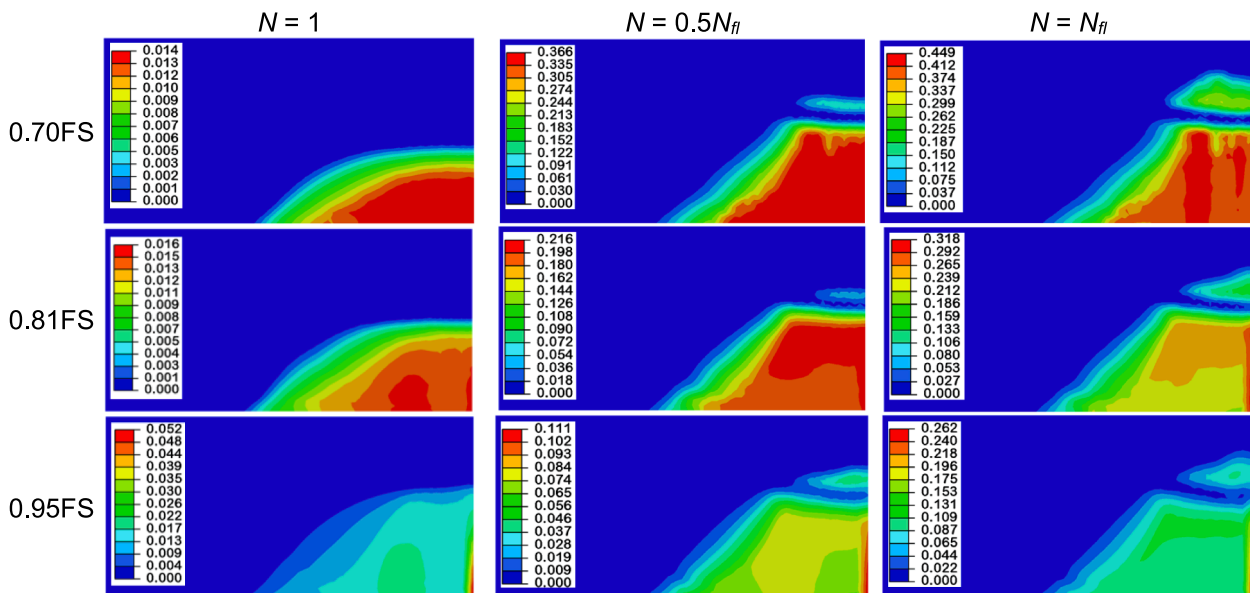

Fig. 36. Maximum total damage variable profiles at different cycles under different stress amplitudes.

cemented materials.

The capabilities of the proposed model are demonstrated and highlighted through satisfactory agreements with experimental outcomes at both constitutive and structural levels, as follows:

- The model describes the material strength loss and energy dissipation, represented by hysteresis loops during cyclic loadings, by the shrinkage and translation of the subloading and bounding surfaces. Thus, the proposed model naturally features an intrinsic hysteresis behaviour without assuming empirical unloading–reloading curves. Consequently, the model effectively captures fatigue damage growth and hysteretic responses at low and high-cycle fatigue problems.
- Two distinct fatigue failure mechanisms in tension-shear and compression-shear regimes are integrated into the model. This is crucial for practical applications wherein arbitrary stress states occur and will be presented in our future work.
- The model reproduces three distinct stages of the fatigue curve by using the phenomenological fatigue damage rule at the meso scale (i. e., the scale of fracture planes) and the interaction between responses of these planes and that of outer bulk.
- The model describes the movement of FPZ in notched and unnotched structures, from initiation to propagation, and fatigue failure during cyclic loadings. Therefore, the development of residual stress and strength zones and the variation in size of the FPZ can be characterised.
- Unlike the thin FPZ observed in the strength test, the FPZ in the fatigue test is larger and exhibits a pronounced curved shape around the notch tip, as well as at the bottom and centre line of unnotched structures.
- The model correctly predicts the fatigue response of cemented materials under variable amplitude loadings, especially sudden overloads, in addition to cyclic constant loading.
- The model effectively captures the significant impact of stress level amplitudes on the fatigue lives of materials, thanks to the adoption of the image and interpolation rules in the proposed model.

CRediT authorship contribution statement

Vinh T. Le: Methodology, Software, Formal analysis, Investigation, Writing – original draft, Visualization. **Ha H. Bui:** Conceptualization, Methodology, Supervision, Software, Investigation, Writing – review & editing, Funding acquisition, Project administration. **Giang D. Nguyen:** Conceptualization, Methodology, Investigation, Writing – review & editing. **Jayantha Kodikara:** Investigation, Writing – review & editing, Funding acquisition. **Didier Bodin:** Investigation, Writing – review & editing. **James Grenfell:** Investigation, Writing – review & editing.

Data availability

No data was used for the research described in the article.

Appendix A. Kinematic rule of the subloading surface

This section presents the kinematic rule of the subloading surface in Section 2.2.

In the normal-shear stress space (Fig. 2a), the vertex (V^K) and centre (C^K) points of the bounding surface can be derived from the geometric property of hyperbola (i.e., $V^K = C^K - a^K$, where $a^K = B$) as follows [34]:

$$C^K = A \tag{54}$$

$$V^K = (1-D)f_t^0 \tag{55}$$

The coordinates of the vertex V^I and centre C^I of the subloading surface (Fig. 2a) can be expressed as (i.e., $V^I = C^I - a^I$, where $a^I = b$):

$$C^I = a + X_n \tag{56}$$

$$V^I = (1-\psi)f_t^0 + X_n \tag{57}$$

Based on the geometric properties of hyperbolas (Fig. 2a), the following relations hold for the bounding and subloading surfaces:

$$V^K - C^K = \frac{a^K}{a^I}\left(V^I - C^I\right) \tag{58}$$

Since the vertices and centres of bounding and subloading surfaces lie on the normal-traction axis in the stress space, the kinematic rules can be formulated by postulating that the relative motion of the point V^I with respect to V^K is directed along χ such that $\dot{V}^I - \dot{V}^K = \chi\dot{\omega}$, where $\dot{\omega}$ is the scalar factor. Furthermore, upon the simultaneous movement and shrinkage of both surfaces, the change in position of V^I and V^K can be established by using the following incremental relations:

$$\dot{V}^I = \dot{C}^I + \frac{\dot{a}^I}{a^I}\left(V^I - C^I\right) \tag{59}$$

$$\dot{V}^K = \dot{C}^K + \frac{\dot{a}^K}{a^K}\left(V^K - C^K\right) \tag{60}$$

Combination of Eqs. (59), (60), and the relation $\dot{V}^I - \dot{V}^K = \chi\dot{\omega}$, the following relation is obtained:

$$\dot{C}^I = \chi\dot{\omega} - \frac{\dot{a}^I}{a^I}(V^I - C^I) + \frac{\dot{a}^K}{a^K}(V^K - C^K) + \dot{C}^K \tag{61}$$

By substituting Eq. (58) into Eq. (61), the kinematic rule of the subloading surface is determined as:

$$\dot{C}^I = \chi\dot{\omega} + (V^I - C^I)\frac{\dot{a}^K - \dot{a}^I}{a^I} + \dot{C}^K \tag{62}$$

The scalar parameter $\dot{\omega}$ in Eq. (62) can be straightforwardly obtained from the consistency condition $\dot{y}_0 = 0$

$$\dot{X}_n = -\frac{\frac{\partial y_0}{\partial t_c}\dot{t}_c}{\frac{\partial y_0}{\partial X_n}} \tag{63}$$

where

$$\frac{\partial y_0}{\partial X_n} = -\frac{\partial y_0}{\partial t_n} \tag{64}$$

$$\dot{C}^I = \dot{X}_n \tag{65}$$

Substituting Eqs. (63) and (65) into Eq. (62) leads to:

$$\dot{\omega} = -\frac{1}{\chi}\left[\frac{\frac{\partial y_0}{\partial t_c}\dot{t}_c}{\frac{\partial y_0}{\partial X_n}} + (V^I - C^I)\frac{\dot{a}^K - \dot{a}^I}{a^I} + \dot{C}^K\right] \tag{66}$$

Finally, the kinematic rule of subloading surface is determined as:

$$\dot{X}_n = \chi\dot{\omega} + (V^I - C^I)\frac{\dot{a}^K - \dot{a}^I}{a^I} + \dot{C}^K \tag{67}$$

Analytical solutions for detecting crack orientation

All solutions of Eq. (36) in Section 3.1 are as follows:
The solution of Eq. $(36)_1$ is:

$$\theta = \frac{1}{2}\tan^{-1}\left(\frac{2\sigma_{xy}}{\sigma_{xx} - \sigma_{yy}}\right) + \frac{k\pi}{2} \tag{68}$$

where $k = 0, 1, 2, 3, \cdots$ as the value of θ is positive.
The left-hand side of Eq. $(36)_2$ can be written as follows:

$$\begin{cases} a_1 cos2\theta + a_2 sin2\theta = Rcos(2\theta - \phi), a_1 \geq 0 \\ a_1 cos2\theta + a_2 sin2\theta = -Rcos(2\theta - \phi), a_1 < 0 \end{cases} \tag{69}$$

where $R = \sqrt{a_1^2 + a_2^2}$, and $\phi = \tan^{-1}(a_2/a_1)$
As a result, Eq. (69) becomes:

$$\begin{cases} cos(2\theta - \phi) = a_3/R, a_1 \geq 0 \\ cos(2\theta - \phi) = -a_3/R, a_1 < 0 \end{cases} \tag{70}$$

The solutions of Eq. (70) are:

$$\begin{cases} \theta = \frac{1}{2}\left[\cos^{-1}(a_3/R) + \phi\right] + k\pi, a_1 \geq 0 \\ \theta = \frac{1}{2}\left[\cos^{-1}(-a_3/R) + \phi\right] + k\pi, a_1 < 0 \end{cases} \tag{71}$$

where $k = 0, 1, 2, 3, \cdots$ as the value of θ is positive. If $|\pm a_3/R| \rangle 1$, there are no solutions for θ.

It should be noted that, the value of θ is in the interval $[0°, 180°]$, hence the boundaries of the closed interval (i.e., $0°$ and $180°$) must be considered when determining the maximum value of y_0^t.

Appendix B. Algorithms for cohesive fatigue model and double-scale framework

Algorithm 1. Stress return algorithm of the cohesive fatigue model

Stress return algorithm

Input value: $\dot{\mathbf{u}}_c$; Output values: $\dot{\mathbf{t}}_c$

Initial value: $D = 0$, ψ_t, threshold=0, bottom=0. Threshold is the fatigue limit depending on the initial value of ψ_t

Constant: K_n, K_s, μ, C^0, f_t^0, α, β, δ_s, δ_f, e_{do}^0

$\mathbf{t}_c^{tr} = \mathbf{t}_c + \Delta\mathbf{t}_c^{tr}$ (calculated from Algorithm 2)

$y^{tr} = \left[(t_n^{tr} - A)/B\right]^2 - (t_s^{tr}/C)^2 - 1$

$y_0^{t\text{-}tr} = \left[(t_n^{tr} - a_t - X_n)/b_t\right]^2 - (t_s^{tr}/c_t)^2 - 1$

$y_0^{b\text{-}tr} = -\left\{\left[(t_n^{tr} - a_b - X_n)/b_b\right]^2 - (t_s^{tr}/c_b)^2 - 1\right\}$

> **If** $y_0^{t\text{-}tr} \geq 0$ **then**
> threshold =1
> **End**

If ($y^{tr} \geq 0$) **then** (On bounding surface)

$$\dot{\lambda} = \frac{-y^{tr}}{\dfrac{\partial y^T}{\partial \mathbf{t}_c}\dfrac{\partial \mathbf{t}_c}{\partial \mathbf{u}_c^p}\dfrac{\partial y}{\partial \mathbf{t}_c} + \dfrac{\partial y^T}{\partial \mathbf{t}_c}\dfrac{\partial \mathbf{t}_c}{\partial D}P + \dfrac{\partial y}{\partial D}P}$$

Compute increment of internal variables: $\dot{\mathbf{u}}_c^p, \dot{D}_s$

Compute correct stress: $\mathbf{t}_c = \mathbf{t}_c^{tr} + \dfrac{\partial \mathbf{t}_c}{\partial \mathbf{u}_c^p}\dot{\mathbf{u}}_c^p + \dfrac{\partial \mathbf{t}_c}{\partial D}\dot{D}_s$

Update internal variables: $\mathbf{u}_c^p = \mathbf{u}_c^p + \dot{\mathbf{u}}_c^p, D = D + \dot{D}_s$

$y = \left[(t_n - A)/B\right]^2 - (t_s/C)^2 - 1$

$y_0^t = \left[(t_n - a_t - X_n)/b_t\right]^2 - (t_s/c_t)^2 - 1$

> **If** ($y_0^t \leq y$) **then** (Top loading surface not allowed to go beyond the bounding surface)
> Reset all memory of past stress reversal events: $\psi_t = D, X_n = 0$
> **End**

Else

> **If** (($y_0^{t\text{-}tr} \geq 0$) and (threshold==1)) **then** (On top loading surface)
>
> Compute internal variables: (IK, OK) or (I_cK_c, O_cK_c), S_K, S_I and then $\dot{\lambda} = \dfrac{-y_0^{t\text{-}tr}}{S_I}$
>
> Compute increment of internal variables: $\dot{\mathbf{u}}_c^f, \dot{D}_f$
>
> Compute correct stress: $\mathbf{t}_c = \mathbf{t}_c^{tr} + \dfrac{\partial \mathbf{t}_c}{\partial \mathbf{u}_c^f}\dot{\mathbf{u}}_c^f + \dfrac{\partial \mathbf{t}_c}{\partial D}\dot{D}_f$
>
> Update internal variables: $\mathbf{u}_c^f = \mathbf{u}_c^f + \dot{\mathbf{u}}_c^f, D = D + \dot{D}_f, e_{do} = e_{do}^0(1 - D)$
>
> Compute and update kinematic variables: $\psi_b = \psi_t + e_{do}, X_n = X_n + \dot{X}_n$
> **Else**
>
> > **If** (($y_0^{b\text{-}tr} \geq 0$) and (threshold==1) **then** (On bottom loading surface)
> >
> > Compute internal variables: (IK, OK) or (I_cK_c, O_cK_c), S_K, S_I and then $\dot{\lambda} = \dfrac{-y_0^{b\text{-}tr}}{S_I}$
> >
> > Compute increment of internal variables: $\dot{\mathbf{u}}_c^f, \dot{D}_f$
> >
> > Compute correct stress: $\mathbf{t}_c = \mathbf{t}_c^{tr} + \dfrac{\partial \mathbf{t}_c}{\partial \mathbf{u}_c^f}\dot{\mathbf{u}}_c^f + \dfrac{\partial \mathbf{t}_c}{\partial D}\dot{D}_f$
> >
> > Update internal variables: $\mathbf{u}_c^f = \mathbf{u}_c^f + \dot{\mathbf{u}}_c^f, D = D + \dot{D}_f, e_{do} = e_{do}^0(1 - D)$
> >
> > Compute and update kinematic variables: $\psi_t = \psi_b - e_{do}, X_n = X_n + \dot{X}_n$
> > **Else** (Elastic step)
> > Update stress and all variables
> > $\mathbf{t}_c = \mathbf{t}_c^{tr}$; $\mathbf{u}_c^p, \mathbf{u}_c^f, D, \psi_t, \psi_b, X_n$ remain unchanged
> > **End**
> **End**
End

Algorithm 2. Implicit algorithm of stress update with input $\Delta\boldsymbol{\varepsilon}$ and output $\Delta\boldsymbol{\sigma}$

---

1. Compute $\mathbf{M}_i$ in Eq. (13) (assume elastic behaviour and replace $\mathbf{K}_k^t$ with $\mathbf{K}_k^{\hat{s}}$, where $\mathbf{K}_k^{\hat{s}}=\mathbf{R}_k^T\mathbf{K}_{ck}^{\hat{s}}\mathbf{R}_k$)
2. With a given $\Delta\boldsymbol{\varepsilon}$, compute trial global displacements $\Delta\mathbf{u}_1^{tr}$ and $\Delta\mathbf{u}_2^{tr}$ according to Eq. (14),
3. Compute trial local displacements $\Delta\mathbf{u}_{c1}^{tr}=\mathbf{R}_1\Delta\mathbf{u}_1^{tr}$ and $\Delta\mathbf{u}_{c2}^{tr}=\mathbf{R}_2\Delta\mathbf{u}_2^{tr}$
4. Compute trial stress $\boldsymbol{\sigma}^{tr}=\boldsymbol{\sigma}+\Delta\boldsymbol{\sigma}^{tr}=\boldsymbol{\sigma}+\mathbf{a}_o\left(\Delta\boldsymbol{\varepsilon}-\frac{1}{L_1}\mathbf{n}_1\Delta\mathbf{u}_1^{tr}-\frac{1}{L_2}\mathbf{n}_1\Delta\mathbf{u}_2^{tr}\right)$
5. Compute trial local tractions $\mathbf{t}_{c1}^{tr}=\mathbf{t}_{c1}+\mathbf{R}_1\mathbf{n}_1^T\Delta\boldsymbol{\sigma}^{tr}$ and $\mathbf{t}_{c2}^{tr}=\mathbf{t}_{c2}+\mathbf{R}_2\mathbf{n}_2^T\Delta\boldsymbol{\sigma}^{tr}$
6. Compute trial local displacements $\mathbf{u}_{c1}^{tr}=\mathbf{u}_{c1}+\Delta\mathbf{u}_{c1}^{tr}$ and $\mathbf{u}_{c2}^{tr}=\mathbf{u}_{c2}+\Delta\mathbf{u}_{c2}^{tr}$
7. Go to Algorithm 1 to compute tractions and internal variables of cracks 1 and 2
8. Compute residual vectors: $\mathbf{r}_1=\mathbf{n}_1^T\boldsymbol{\sigma}^{tr}-\mathbf{R}_1\mathbf{t}_{c1}$ and $\mathbf{r}_2=\mathbf{n}_2^T\boldsymbol{\sigma}^{tr}-\mathbf{R}_2\mathbf{t}_{c2}$
9. While $\left(\frac{\|\mathbf{r}_1\|}{\|\mathbf{t}_{c1}\|}\geq\text{tol or}\frac{\|\mathbf{r}_2\|}{\|\mathbf{t}_{c2}\|}\geq\text{tol}\right)$ do
10. Compute $\mathbf{M}_i$ in Eq. (13) (replace $\mathbf{K}_k^t$ with $\mathbf{K}_k^{\hat{s}}$ which is calculated with new updated internal variables)
11. Compute global displacements $\delta\mathbf{u}_1$ and $\delta\mathbf{u}_2$ according to Eq. (45)
12. Compute local displacements $\delta\mathbf{u}_{c1}=\mathbf{R}_1\delta\mathbf{u}_1$ and $\delta\mathbf{u}_{c2}=\mathbf{R}_2\delta\mathbf{u}_2$
13. Compute local trial tractions $\mathbf{t}_{c1}^{tr}=\mathbf{t}_{c1}+\mathbf{K}_{c1}^{\hat{s}}\delta\mathbf{u}_{c1}$ and $\mathbf{t}_{c2}^{tr}=\mathbf{t}_{c2}+\mathbf{K}_{c2}^{\hat{s}}\delta\mathbf{u}_{c1}$
14. Go to Algorithm 1 to compute tractions and internal variables of cracks 1 and 2
15. Update local displacements $\mathbf{u}_{c1}=\mathbf{u}_{c1}+\delta\mathbf{u}_{c1}$ and $\mathbf{u}_{c2}=\mathbf{u}_{c1}+\delta\mathbf{u}_{c2}$
16. Compute $\delta\boldsymbol{\sigma}=-\frac{1}{L_1}\mathbf{a}_o\mathbf{n}_1\delta\mathbf{u}_1-\frac{1}{L_2}\mathbf{a}_o\mathbf{n}_2\delta\mathbf{u}_2$
17. Update stress $\boldsymbol{\sigma}$, and residual vectors $\mathbf{r}_k$
18. End while

References

[1] Allegri G. A unified formulation for fatigue crack onset and growth via cohesive zone modelling. J Mech Phys Solids 2020;138:103900.

[2] Alliche A. Damage model for fatigue loading of concrete. Int J Fatigue 2004;26(9): 915–21.

[3] Aslani F, Jowkarmeimandi R. Stress–strain model for concrete under cyclic loading. Mag Concr Res 2012;64(8):673–85.

[4] Austroads. (2014). Cemented Materials Characterisation: Final Report. Austroads technical report, Austroads, Sydney, Australia AP-R462-14.

[5] Baktheer A, Aguilar M, Chudoba R. Microplane fatigue model MS1 for plain concrete under compression with damage evolution driven by cumulative inelastic shear strain. Int J Plast 2021;143:102950.

[6] Baktheer A, Becks H. Fracture mechanics based interpretation of the load sequence effect in the flexural fatigue behavior of concrete using digital image correlation. Constr Build Mater 2021;307:124817.

[7] Baktheer A, Chudoba R. Pressure-sensitive bond fatigue model with damage evolution driven by cumulative slip: Thermodynamic formulation and applications to steel-and FRP-concrete bond. Int J Fatigue 2018;113:277–89.

[8] Bazant ZP, Xu K. Size effect in fatigue fracture of concrete. ACI Mater J 1991;88(4): 390–9.

[9] Breccolotti M, Bonfigli MF, D'Alessandro A, Materazzi AL. Constitutive modeling of plain concrete subjected to cyclic uniaxial compressive loading. Constr Build Mater 2015;94:172–80.

[10] Bui HH, Nguyen GD. Smoothed particle hydrodynamics (SPH) and its applications in geomechanics: From solid fracture to granular behaviour and multiphase flows in porous media. Comput Geotech 2021;138:104315.

[11] Chen X, Xu L, Shi D, Chen Y, Zhou W, Wang Q. Experimental study on cyclic tensile behaviour of concrete under various strain rates. Mag Concr Res 2018;70(2): 55–70.

[12] Cho BH, Nam BH, Khawaji M. Flexural fatigue behaviors and damage evolution analysis of edge-oxidized graphene oxide (EOGO) reinforced concrete composites. Cem Concr Compos 2021;122:104082.

[13] Das A, Tengattini A, Nguyen GD, Viggiani G, Hall SA, Einav I. A thermomechanical constitutive model for cemented granular materials with quantifiable internal variables. Part II–validation and localization analysis. J Mech Phys Solids 2014;70: 382–405.

[14] Desmorat R, Ragueneau F, Pham H. Continuum damage mechanics for hysteresis and fatigue of quasi-brittle materials and structures. Int J Numer Anal Meth Geomech 2007;31(2):307–29.

[15] Eliáš J, Le J-L. Modeling of mode-I fatigue crack growth in quasibrittle structures under cyclic compression. Eng Fract Mech 2012;96:26–36.

[16] Elices M, Guinea G, Gomez J, Planas J. The cohesive zone model: advantages, limitations and challenges. Eng Fract Mech 2002;69(2):137–63.

[17] Fujita Y, Ishimaru R, Hanai S, Suenaga Y. Study on internal friction angle and tensile strength of plain concrete. Proceedings of fracture mechanics of concrete structures FRAMCOS 1998;3:325–34.

[18] Gan Y, Zhang H, Zhang Yu, Xu Y, Schlangen E, van Breugel K, et al. Experimental study of flexural fatigue behaviour of cement paste at the microscale. Int J Fatigue 2021;151:106378.

[19] Gopalaratnam V, Shah SP. Softening response of plain concrete in direct tension. Journal Proceedings 1985.

[20] Hillerborg A, Modéer M, Petersson P-E. Analysis of crack formation and crack growth in concrete by means of fracture mechanics and finite elements. Cem Concr Res 1976;6(6):773–81.

[21] Isojeh B, El-Zeghayar M, Vecchio FJ. High-cycle fatigue life prediction of reinforced concrete deep beams. Eng Struct 2017;150:12–24.

[22] Jimenez S, Duddu R. On the parametric sensitivity of cohesive zone models for high-cycle fatigue delamination of composites. Int J Solids Struct 2016;82:111–24.

[23] Jin G-L, Zhang Z-X, Huang X-M. Fatigue Cracking Analysis of Asphalt Concrete Based on Coupled XFEM-Continuum Damage Mechanics Method. J Mater Civ Eng 2021;33(1):04020425.

[24] Jin G, Huang X. Predicting Fatigue Damage of Asphalt Concrete Using a Cohesive Zone Model. Int J Pavement Res Technol 2014;7(5).

[25] Kachkouch FZ, Noberto CC, de Albuquerque Lima Babadopulos LF, Melo ARS, Machado AML, Sebaibi N, et al. Fatigue behavior of concrete: A literature review on the main relevant parameters. Constr Build Mater 2022;338:127510.

[26] Keerthana K, Kishen JMC. Micromechanics of fracture and failure in concrete under monotonic and fatigue loadings. Mech Mater 2020;148:103490.

[27] Kirane K, Bažant ZP. Microplane damage model for fatigue of quasibrittle materials: Sub-critical crack growth, lifetime and residual strength. Int J Fatigue 2015;70:93–105.

[28] Kirane K, Bažant ZP. Size effect in Paris law and fatigue lifetimes for quasibrittle materials: Modified theory, experiments and micro-modeling. Int J Fatigue 2016; 83:209–20.

[29] Kolymbas D. Kinematics of shear bands. Acta Geotech 2009;4(4):315–8.

[30] Kuna M, Roth S. General remarks on cyclic cohesive zone models. Int J Fract 2015; 196(1–2):147–67.

[31] Le LA, Nguyen GD, Bui HH, Sheikh AH, Kotousov A. Localised failure mechanism as the basis for constitutive modelling of geomaterials. Int J Eng Sci 2018;133: 284–310.

[32] Le LA, Nguyen GD, Bui HH, Sheikh AH, Kotousov A. Incorporation of micro-cracking and fibre bridging mechanisms in constitutive modelling of fibre reinforced concrete. J Mech Phys Solids 2019;133:103732.

[33] Le LA, Nguyen GD, Bui HH, Sheikh AH, Kotousov A, Khanna A. Modelling jointed rock mass as a continuum with an embedded cohesive-frictional model. Eng Geol 2017;228:107–20.

[34] Le VT, Tran KM, Kodikara J, Bodin D, Grenfell J, Bui HH. A two-surface contact model for DEM and its application to model fatigue crack growth in cemented materials. Int J Plast 2023;166:103650.

[35] Leciñana I, Zurbitu J, Renart J, Turon A. A robust fatigue parameter determination method for a local fatigue cohesive zone model. Int J Fatigue 2023;171:107582.

[36] Lee M, Barr B. An overview of the fatigue behaviour of plain and fibre reinforced concrete. Cem Concr Compos 2004;26(4):299–305.

[37] Liang J, Ren X, Li J. A competitive mechanism driven damage-plasticity model for fatigue behavior of concrete. Int J Damage Mech 2016;25(3):377–99.

[38] Liu Xi, Wang R, Hu D, Zhang L, Chen G. Degradation analysis on high-cycle bending fatigue for woven SiC/SiC composites based on Wiener process model. Mater Des 2021;198:109295.

[39] Mai SH, Le-Corre F, Forêt G, Nedjar B. A continuum damage modeling of quasi-static fatigue strength of plain concrete. Int J Fatigue 2012;37:79–85.

[40] Mallikarachchi HE. Constitutive Modelling of Shear Localisation in Saturated Dilative Sand. University of Cambridge]; 2019.

[41] Marigo J. Modelling of brittle and fatigue damage for elastic material by growth of microvoids. Eng Fract Mech 1985;21(4):861–74.

[42] Nguyen GD, Bui HH. A thermodynamics-and mechanism-based framework for constitutive models with evolving thickness of localisation band. Int J Solids Struct 2020;187:100–20.

[43] Nguyen GD, Einav I, Guiamatsia I. On the partition of fracture energy in constitutive modelling of quasi-brittle materials. Eng Fract Mech 2012;79:225–44.

[44] Nguyen GD, Einav I, Korsunsky AM. How to connect two scales of behaviour in constitutive modelling of geomaterials. Géotechnique Letters 2012;2(3):129–34.

[45] Nguyen GD, Korsunsky AM. Damage-plasticity modelling of concrete: Calibration of parameters using separation of fracture energy. Int J Fract 2006;139(2):325–32.

[46] Nguyen GD, Korsunsky AM, Einav I. A constitutive modelling framework featuring two scales of behaviour: fundamentals and applications to quasi-brittle failure. Eng Fract Mech 2014;115:221–40.

[47] Nguyen GD, Nguyen CT, Bui HH, Nguyen VP. Constitutive modelling of compaction localisation in porous sandstones. Int J Rock Mech Min Sci 2016;83:57–72.

[48] Nguyen GD, Nguyen CT, Nguyen VP, Bui HH, Shen L. A size-dependent constitutive modelling framework for localised failure analysis. Comput Mech 2016;58(2):257–47.

[49] Nguyen NH, Bui HH, Kodikara J, Arooran S, Darve F. A discrete element modelling approach for fatigue damage growth in cemented materials. Int J Plast 2019;112:68–88.

[50] Nguyen O, Repetto E, Ortiz M, Radovitzky R. A cohesive model of fatigue crack growth. Int J Fract 2001;110(4):351–69.

[51] Papa E, Taliercio A. Anisotropic damage model for the multiaxial static and fatigue behaviour of plain concrete. Eng Fract Mech 1996;55(2):163–79.

[52] Phan DG, Nguyen GD, Bui HH, Bennett T. The effect of hydro-mechanical coupling on the onset and orientation of localisation bands in partially saturated soils. Int J Plast 2023;162:103551.

[53] Pietruszczak S, Haghighat E. Modeling of deformation and localized failure in anisotropic rocks. Int J Solids Struct 2015;67:93–101.

[54] Ray S, Kishen JC. Fatigue crack propagation model for plain concrete–An analogy with population growth. Eng Fract Mech 2010;77(17):3418–33.

[55] Ren X, Wei X, Ballarini R. A Temporal Multiscale Model for Fatigue Damage of Concrete. J Eng Mech 2022;148(3):04021163.

[56] Rezazadeh M, Carvelli V. A damage model for high-cycle fatigue behavior of bond between FRP bar and concrete. Int J Fatigue 2018;111:101–11.

[57] Rudnicki JW, Rice J. Conditions for the localization of deformation in pressure-sensitive dilatant materials. J Mech Phys Solids 1975;23(6):371–94.

[58] Sima JF, Roca P, Molins C. Cyclic constitutive model for concrete. Eng Struct 2008;30(3):695–706.

[59] Skarżyński Ł, Marzec I, Tejchman J. Fracture evolution in concrete compressive fatigue experiments based on X-ray micro-CT images. Int J Fatigue 2019;122:256–72.

[60] Song Z, Konietzky H, Herbst M. Bonded-particle model-based simulation of artificial rock subjected to cyclic loading. Acta Geotech 2019;14(4):955–71.

[61] Sounthararajah A, Bui HH, Nguyen N, Jitsangiam P, Kodikara J. Early-age fatigue damage assessment of cement-treated bases under repetitive heavy traffic loading. J Mater Civ Eng 2018;30(6):04018079.

[62] Tran HT, Wang Y, Nguyen GD, Kodikara J, Sanchez M, Bui HH. Modelling 3D desiccation cracking in clayey soils using a size-dependent SPH computational approach. Comput Geotech 2019;116:103209.

[63] Tsutsumi S, Fincato R. Cyclic plasticity model for fatigue with softening behaviour below macroscopic yielding. Mater Des 2019;165:107573.

[64] Turon A, Costa J, Camanho P, Dávila C. Simulation of delamination in composites under high-cycle fatigue. Compos A Appl Sci Manuf 2007;38(11):2270–82.

[65] Van Paepegem W, Degrieck J. Fatigue degradation modelling of plain woven glass/epoxy composites. Compos A Appl Sci Manuf 2001;32(10):1433–41.

[66] Vicente MA, Ruiz G, Gonzalez DC, Minguez J, Tarifa M, Zhang X. CT-Scan study of crack patterns of fiber-reinforced concrete loaded monotonically and under low-cycle fatigue. Int J Fatigue 2018;114:138–47.

[67] Wang R, Liu Yu, Mao J, Liu Z, Hu D. Cyclic cohesive zone model damage parameter acquisition for fatigue crack growth considering crack closure effect. Int J Fatigue 2022;163:107021.

[68] Wang Y. A new insight into the three phases of secant stiffness degradation of concrete under fatigue loading. Int J Fatigue 2023;167:107323.

[69] Wang Y, Li J. A two-scale stochastic damage model for concrete under fatigue loading. Int J Fatigue 2021;153:106508.

[70] Wang Y, Tran HT, Nguyen GD, Ranjith PG, Bui HH. Simulation of mixed-mode fracture using SPH particles with an embedded fracture process zone. Int J Numer Anal Meth Geomech 2020;44(10):1417–45.

[71] Williams J, Hadavinia H. Analytical solutions for cohesive zone models. J Mech Phys Solids 2002;50(4):809–25.

[72] Wong R, Ma S, Wong R, Chau KT. Shear strength components of concrete under direct shearing. Cem Concr Res 2007;37(8):1248–56.

[73] Xie Di, Zhang W, Lyu Z, Liaw PK, Tran H, Chew HB, et al. Plastic anisotropy and twin distributions near the fatigue crack tip of textured Mg alloys from in situ synchrotron X-ray diffraction measurements and multiscale mechanics modeling. J Mech Phys Solids 2022;165:104936.

[74] Xu Y, Yuan H. Computational analysis of mixed-mode fatigue crack growth in quasi-brittle materials using extended finite element methods. Eng Fract Mech 2009;76(2):165–81.

[75] Yang B, Mall S, Ravi-Chandar K. A cohesive zone model for fatigue crack growth in quasibrittle materials. Int J Solids Struct 2001;38(22–23):3927–44.

[76] Zhang L, Gao Z, Haynes RA, Henry TC, Yu W. An anisotropic continuum damage model for high-cycle fatigue. Mech Adv Mater Struct 2020:1–15.

[77] Zhang P, Ren Q, Lei D. Hysteretic model for concrete under cyclic tension and tension-compression reversals. Eng Struct 2018;163:388–95.

[78] Zhao Qi, Abdel Wahab M, Ling Y, Liu Z. Fatigue crack propagation within Al-Cu-Mg single crystals based on crystal plasticity and XFEM combined with cohesive zone model. Mater Des 2021;210:110015.

[79] Zhao X, Dong Q, Chen X, Han H, Zhang T. Evaluation of fatigue performance of cement-treated composites based on residual strength through discrete element method. Constr Build Mater 2021;306:124904.

[80] Zhao X, Dong Q, Chen X, Xiao Y, Zheng D. Fatigue damage numerical simulation of cement-treated base materials by discrete element method. Constr Build Mater 2021;276:122142.